CZECH TECHNICAL UNIVERSITY IN PRAGUE
Faculty of Nuclear Sciences and Physical Engineering
Department of Physics

Research Project

Coherent photoproduction of ψ(2S) vector mesons in Pb–Pb UPC

Bc. Zuzana Gajdošová

Supervisor: doc. Jesús Guillermo Contreras Nuño, Ph.D.

Prague, 2018

ČESKÉ VYSOKÉ UČENÍ TECHNICKÉ V PRAZE
FAKULTA JADERNÁ A FYZIKÁLNĚ INŽENÝRSKÁ
PRAHA 1 - STARÉ MĚSTO, BŘEHOVÁ 7 - PSČ 115 19

Katedra: fyziky **Akademický rok:** 2016/2017

VÝZKUMNÝ ÚKOL

Student: Bc. Zuzana Gajdošová

Obor: **Experimentální jaderná a částicová fyzika**

Vedoucí úkolu: doc. Guillermo Contreras Nuño, Ph.D.

Konzultant: Mgr. Michal Broz, Ph.D.

Název úkolu (česky/anglicky): Koherentní fotoprodukce vektorových mezonů Psi(2S) v Pb-Pb UPC / Coherent photoproduction of Psi(2S) vector mesons in Pb-Pb UPC

Pokyny pro vypracování:
1. Zpracujte rešerši těchto témat:
    a) Charakteristika UPC
    b) Experiment ALICE na urychlovači LHC
2. Studujte rozpadové kanály Psi(2S)
3. Použijte Monte Carlo simulace pro koherentní fotoprodukce Psi(2S)
4. Studujte efektivitu, akceptanci a účinný průřez
5. Studujte systematické neurčitosti koherentní fotoprodukce Psi(2S)

Součástí zadání výzkumného úkolu je jeho uložení na webové stránky katedry fyziky.

Tato práce bude vypracována v rámci kolaborace ALICE, která zahrnuje instituce ze 42 krajin, proto bude psána v anglickém jazyce, aby byla přístupna všem členům kolaborace.

Literatura:
[1] J. Adam, et al. [ALICE collaboration], Coherent ψ(2S) photo-production in ultra-peripheral Pb-Pb collisions at $\sqrt{s}_{\rm NN}$ = 2.76 TeV, Phys.Lett. B751 358-370 (2015).

[2] K. Aamodt, et al. [ALICE collaboration], The ALICE experimetn at the CERN LHC, JINST 3 S08002 (2008).

[3] J. G. Contreras, J. D. Tapaki, Ultra-peripheral heavy-ion collisions at the LHC, Mod. Phys. A30 1542012 (2015).

Prohlášení

Prohlašuji, že jsem svůj výzkumný úkol vypracovala samostatně a použila jsem pouze podklady (literaturu, projekty, SW atd.) uvedené v přiloženém seznamu.

Nemám závažný důvod proti použití tohoto školního díla ve smyslu §60 Zákona č.121/1200Sb., o právu autorském, o právech souvisejících s právem autorským a o změně některých zákonů (autorský zákon).

V Praze dne ....

Acknowledgements

I would like to express my gratitude to my supervisor, doc. Jesús Guillermo Contreras Nuño Ph.D., for his support, interest in my work and for his patience and bright advices. Special thanks go to Mgr. Michal Broz, Ph.D., for preparing the data sample and also for his valuable advice and answers to all my questions. Of course I would like to also thank to my sister Katarína Gajdošová for her willingness to help, my parents, grandmother and Javier Martínez Ruiz, for their great support during the realisation of this work.

Název práce: **Koherentní fotoprodukce vektorových mezonů ψ(2S) v Pb–Pb UPC**
Autor: Bc. Zuzana Gajdošová

Obor: Experimentální jaderná a částicová fyzika

Druh práce: Výzkumný úkol

Vedoucí práce: doc. Jesús Guillermo Contreras Nuño, Ph.D.
Katedra fyziky, Fakulta jaderná a fyzikálně inženýrská,
České vysoké učení technické v Praze.

Abstrakt:

Jedna z mnoha otevřených otázek současné QCD je příčina jevu jaderného stínění. Abychom mohli porozumět tomuto jevu, je důležité studovat gluonové distribuce v jádře při malém x. Existuje mnoho různych modelů, snažících se popsat tyto jevy v QCD, které je potřeba experimentálně ověřit. Jeden z procesů vhodných pro zkoumání gluonové distribuce v jádře je koherentní fotoprodukce vektorového mezonu. Měření účinného průřezu tohoto procesu může sloužit jako ověření platnosti jedné nebo více teoretických předpovědí fenoménů v QCD.

V tomto výzkumném úkolu jsme připravili nástroje potřebné pro výpočet účinného průřezu koherentní fotoprodukce vektorového mezonu ψ(2S), jako jsou určení výtěžku ψ(2S), vypočítaní luminozity, určení součinu akceptance a efektivity a odhad souvisejících systematických chyb. Studium, prezentované v této práci bylo provedeno na datech ze srážek Pb–Pb při těžišťové energii $\sqrt{s_{\mathrm{NN}}} = 5.02$ TeV, která byla nabrána během Run 2 na LHC s detektorem ALICE v střední rapiditě. Měření účinného průřezu v této rapiditě s téměř dojnásobnou energií než byla k dispozici v Run 1 zajistí důležitý pokrok při hledání původu stínění.

Klíčová slova: ultra-periferální srážky, ALICE, ψ(2S), luminozita, akceptance a efektivita, Monte Carlo simulace

Title: **Coherent photoproduction of ψ(2S) vector mesons in Pb–Pb UPC**
Author: Bc. Zuzana Gajdošová

Specialization: Experimental nuclear and particle physics

Supervisor: doc. Jesús Guillermo Contreras Nuño, Ph.D.
Department of physics, Faculty of Nuclear Sciences and Physical Engineering, Czech Technical University in Prague.

Abstract:

One of the open questions in QCD today is the cause of the shadowing phenomenon in nuclei. To understand this phenomenon it is necessary to study gluon distributions in nuclei at small x. There are several models trying to describe such phenomenon in QCD which have to be experimentally scrutinised and confirmed. One of the suitable processes to investigate gluon distributions in nuclei is the coherent photoproduction of a vector meson. The measurement of its cross section can serve as a verification of one or more theoretical predictions of this QCD phenomenon.

During this Research Project tools were prepared for the calculation of the cross section of the coherent photoproduction of the vector meson ψ(2S), such as determination of the

yield of ψ(2S), the calculation of luminosity, the determination of the product of the acceptance and efficiency and estimation of some related systematic uncertainties. The studies presented here were performed with data from Pb–Pb collisions at a centre-of-mass energy $\sqrt{s_{\rm NN}} = 5.02$ TeV collected during the Run 2 data-taking period at the LHC with the ALICE detector at mid-rapidity. The measurement of the cross section at this rapidity region and with almost 2 times higher energies than in Run 1 will provide an important contribution to the search for the origin of the shadowing.

Keywords: ultra-peripheral collisions, ALICE, ψ(2S), luminosity, acceptance and efficiency, Monte Carlo simulation

Contents

List of Figures

List of Tables

Chapter 1

Introduction

This Research Project is dedicated to the study of the coherent photoproduction of the vector meson $\psi(2S)$ in ultra-peripheral collisions (UPC) of Pb–Pb ions at the LHC with the detector ALICE in the central rapidity region. The accelerated charged nuclei, colliding at a centre-of-mass energy per nucleon pair of $\sqrt{s_{\mathrm{NN}}} = 5.02$ TeV carry boosted electromagnetic fields, thus in UPC we can observe photon-photon or photon-nucleus interactions which gives us a unique opportunity to study phenomena in QCD, such as shadowing and saturation.

This work is organised as follows. Chapter 2 introduces the basic characteristics of UPC. It defines the different types of photoproduction interactions including the coherent and incoherent production of vector mesons, it presents the kinematics for these processes, and finally presents a brief overview of small-x physics.

In Chap. 3 the ALICE detector is presented. Special attention is given to the characteristics of the detectors used in the analysis of the data. The ALICE trigger system is also presented here.

After that, in Chap. 4, the latest available results from Run 2 in ALICE on charmonium photoproduction are presented. In particular, the following measurements are described: the photoproduction of the J/ψ vector meson at forward and central rapidity and then also the study of the $\psi(2S)$ vector meson at central rapidity.

After these introductory chapters, we proceed in Chap. 5 to discuss the main results of this Research Project, namely the analysis of the data on the coherent photoproduction of the vector meson $\psi(2S)$ at central rapidity with Pb-Pb collisions at a centre-of-mass energy of $\sqrt{s_{\mathrm{NN}}} = 5.02$ TeV with the ALICE deterctor. The analysed data were collected during the so-called Run 2 of the LHC. We study the reconstruction of the $\psi(2S)$ signal using the following decay channels: $\psi(2S) \to l^+l^-$ where l stands for either and electron or a muon, and $\psi(2S) \to \mathrm{J}/\psi\pi^+\pi^-$. The chapter covers the selection criteria through the extraction of the signal, Monte Carlo simulations, the study of the acceptance-times-efficiency product and systematic uncertainties.

The results from this chapter are then summarised and discussed in the last chapter of this thesis.

Chapter 2

Introduction to ultra-peripheral collisions

2.1 Ultra-peripheral collisions

In 1924 Enrico Fermi developed a method which described fast charged particles carrying electromagnetic fields as a flux of virtual photons. Later on, this method was applied to relativistic heavy ions [1]. When two relativistic heavy ions – each the carrier of a cloud of virtual photons – pass at an impact parameter b that is larger than the sum of their radii, the only way the heavy ions can interact is via their clouds of virtual photons, see Fig. 2.1. Since the weak and gravitational interactions are weak in comparison with the electromagnetic and strong interactions, they do not play any role in the following discussions.

Although hadronic interactions could be present in the collision, they are practically all suppressed since the range of the strong force is about 1 femtometer and we are referring to larger impact parameters. So the dominant interaction in these processes has an electromagnetic component. This type of processes are called ultra-peripheral collisions (UPC).

The intensity of the photon flux is proportional to Z^2 with Z the atomic number of the ion. It is clear that any charged particle might be used as a projectile for UPC, but the ions with higher Z yield a more intense flux. In this Research Project we are working with ions of Pb as a target and as a projectile in UPC.

Since we are talking about relativistic heavy ions, the maximum energy ω^{max} of the photon flux is limited by the boost of the source in the laboratory frame, Eq. (2.1), which is several TeV at the LHC:

$$\omega^{max} = \frac{\hbar}{\Delta t} \sim \frac{\gamma \hbar v}{b}, \tag{2.1}$$

where Δt is the interaction time, b the impact parameter, γ the Lorentz factor and v the projectile velocity. These photons are quasi-real with their virtualities are given by $Q^2 = -q^2 \approx (\hbar/R_A)^2$, where R_A is the nuclear radius [2].

The interaction between target and projectile may occur in different ways. The high energy photon emitted from the projectile can interact directly with the target, see example in Fig. 2.2a. The cross section for this type of photoproduction is

$$\sigma_X = \int d\omega \frac{n(\omega)}{\omega} \sigma_X^{\gamma}(\omega), \tag{2.2}$$

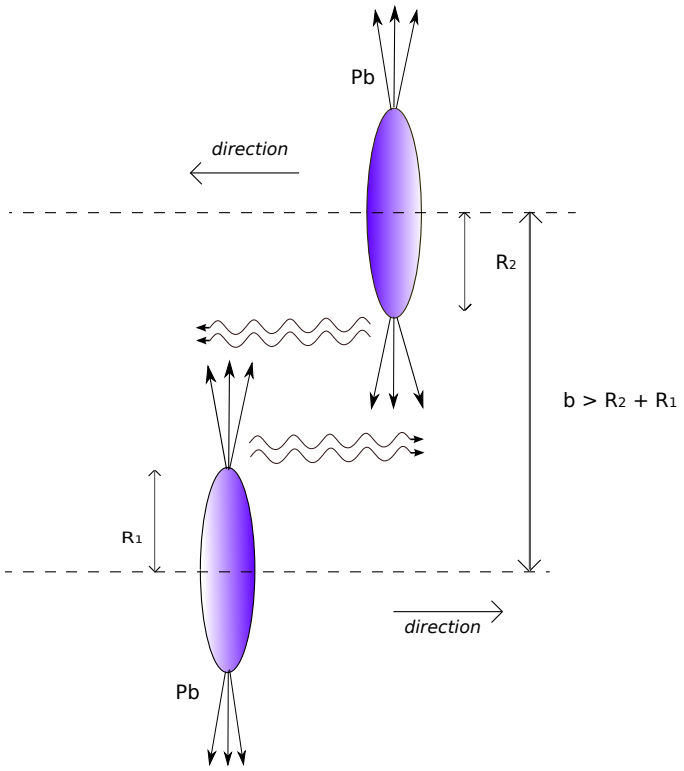

Figure 2.1: Diagram of an interaction of heavy ions of Pb via the cloud of virtual photons, UPC. The gradient of the colour represents the direction of movement of the Pb.

where $\sigma_X^{\gamma}(\omega)$ is the photon–target cross section, ω is the energy of photon and $n(\omega)$ is the number of photons [2].

Another way that an interaction may occur is as $\gamma\gamma \to X$, i.e. the high energy photon emitted from the target interacts directly with another photon emitted from the projectile producing the final state X, Fig. 2.2b. The cross section of this process is analogous to Eq. (2.2):

$$\sigma_X = \int d\omega_1 d\omega_2 \frac{n(\omega_1)}{\omega_1} \frac{n(\omega_2)}{\omega_2} \sigma_X^{\gamma\gamma}(\omega_1, \omega_2), \tag{2.3}$$

where magnitudes are the same as in Eq. (2.2) with the difference of the two-photon cross section $\sigma_X^{\gamma\gamma}(\omega_1, \omega_2)$ [2].

Here, we are interested in Pb–Pb interactions where one of the incoming ions emits a quasi-real photon which then interacts with the other incoming ion to produce a vector meson. In particular, we are interested in photoproduction of the ψ(2S) vector meson off a Pb target. This process is illustrated in Fig. 2.3 in more detail. The photon emitted from the target fluctuates into a quark-antiquark pair, in our case the $q\bar{q}$ pair is charm-anticharm. This $c\bar{c}$ colour dipole consequently interacts with the target through the interchange of a colourless configuration of gluons producing a vector meson, in this case a ψ(2S), with small transverse momentum. One can apply perturbative QCD to compute this process, but a convenient reference frame must be used since the lifetime of $q\bar{q}$ pair must be long enough to be able to interact with the target.

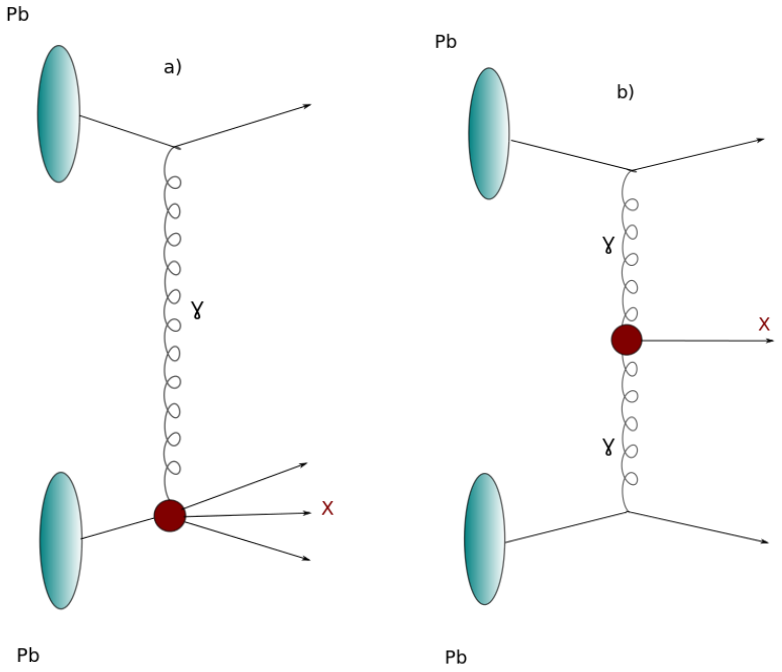

Figure 2.2: Illustration of the manner how the nuclei interact via photons.

2.2 The $\psi(2S)$ vector meson

The particle $\psi(3695)$ was discovered at the experiment SPEAR at the Stanford Linear Accelerator Center, SLAC-LBL on November 25, 1974 [3]. The mass of the newly discovered particle was estimated to be $m_{\psi(3695)} = (3.695 \pm 0.004)$ GeV/c^2. Since then the mass of the $\psi(2S)$ was constrained to the current value of $3686.109^{+0.012}_{-0.014}$ MeV/c^2 and its full width is $\Gamma = (299 \pm 8)$ keV [4].

The $\psi(2S)$ can be measured in different decay channels; direct decay into two leptons (electron-positron or μ^+-μ^-) $\psi(2S) \rightarrow l^- l^+$ or another frequently used channel is the channel where the final state consist of four particles, $\psi(2S) \rightarrow J/\psi + \pi^-\pi^+$, where $J/\psi \rightarrow l^- l^+$. The corresponding decay channels are reported in Tab. 2.1.

Decay channel	Branching ratio
$\psi(2S) \rightarrow J/\psi + \pi^-\pi^+$	$34.00\% \pm 0.40\%$
$J/\psi \rightarrow \mu^- + \mu^+$	$5.93\% \pm 0.06\%$
$J/\psi \rightarrow e^- + e^+$	$5.94\% \pm 0.06\%$

Table 2.1: Branching ratio of different $\psi(2S)$ decay channels [4].

2.3 Types of exclusive photoproduction of a vector meson

The exclusive photoproduction of the vector meson can be either coherent or incoherent. Coherent denotes the process where the colour dipole interacts with the whole colour field of the target, i.e. the emitted photon has to have a wavelength greater or equal to the nuclear radius [1]. Its main characteristic is the small transverse momentum $p_T \approx 60$

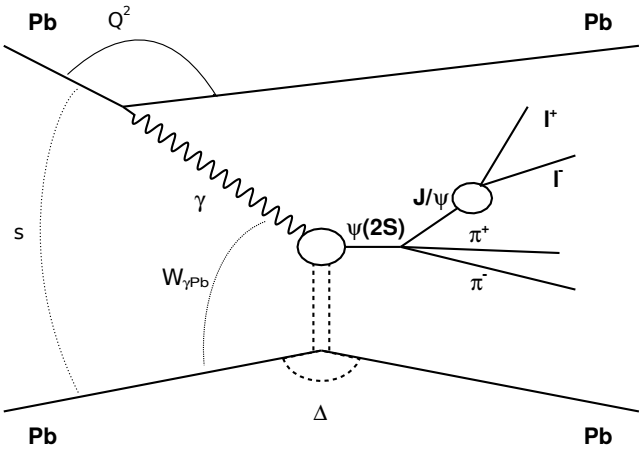

Figure 2.3: Diagram for the coherent photoproduction off a lead nucleus of a ψ(2S) vector meson and its subsequent decay into a J/ψ and two pions.

MeV/c of the final state. The nuclei normally do not break up, however an additional interchange of photons may lead to the break up or disintegration of at least one of the nuclei. On the other hand there is incoherent photoproduction which means that the colour dipole couples to a single nucleon inside the target nucleus. It is characterised by higher transverse momentum of the vector meson $p_T \approx 500$ MeV/c. In this case the nucleus breaks up almost every time.

An example of a photoproduced ψ(2S) in Pb–Pb collisions at $\sqrt{s_{\rm NN}} = 2.76$ TeV is shown in Fig. 2.4. Given the kinematics of the decay products, the leptons from the J/ψ have more transverse momentum than the pions, and thus they curve less in the magnetic field in which the trackers are immersed. Furthermore, the particle-identification capabilities of ALICE, allow us to distinguish electrons from muons in this kinematic region. So, the red lines in the figure correspond to muons and the yellow lines to pions. This interaction is thus called *exclusive photoproduction*. The term exclusive refers to the production of only one vector meson in the interaction of the colour dipole with the target nucleus or the target nucleon for coherent or incoherent processes, respectively.

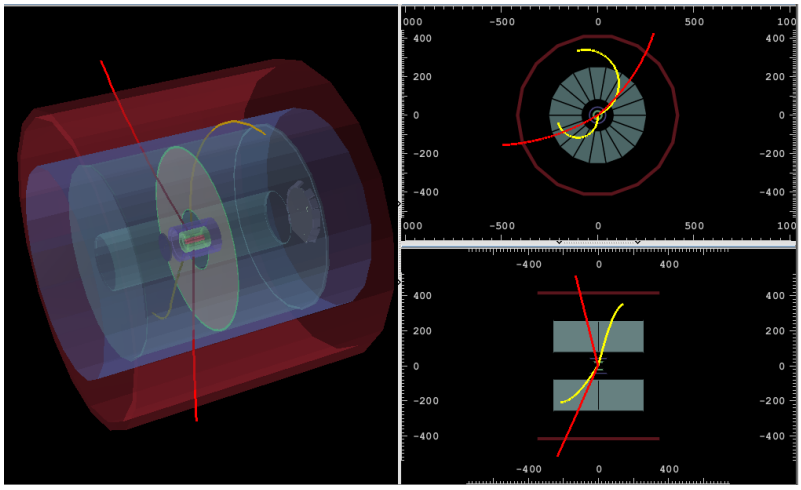

Figure 2.4: An event for coherent photoproduction of a ψ(2S) from Pb–Pb collision in ALICE at $\sqrt{s_{\rm NN}} = 2.76$ TeV from Run 1. The red lines correspond to the $\mu^{\pm}$ and the yellow lines to the $\pi^{\pm}$.

2.4 Kinematics of exclusive photoproduction of a vector meson

Two variables have to be measured to determine the kinematics of the process. In our case, they are p_T and rapidity y. The rapidity is defined as following

$$y = \ln\frac{(p_0 + p_z)}{(p_0 - p_z)}, \tag{2.4}$$

where p_0 and p_z refer to the zero and third entries of the four momenta of the vector meson, respectively. The kinematical description of the process depicted in Fig. 2.3 is provided by the centre-of-mass energy of the photon-target system, $W_{\gamma\mathrm{Pb}}$, as

$$(W_{\gamma\mathrm{Pb}})^2_{\pm} = \mathrm{M}\exp(\pm|y|)\sqrt{s_{\mathrm{NN}}}, \tag{2.5}$$

where M is the mass of the vector meson.

The differential cross section for the coherent photoproduction of the vector meson in a Pb–Pb UPC is

$$\frac{d\sigma_{\mathrm{PbPb}}(y)}{dy} = N_{\gamma/\mathrm{Pb}}(y, \mathrm{M})\sigma_{\gamma/\mathrm{Pb}}(\mathrm{y}) + \mathrm{N}_{\gamma/\mathrm{Pb}}(-\mathrm{y}, \mathrm{M})\sigma_{\gamma/\mathrm{Pb}}(-\mathrm{y}), \tag{2.6}$$

where the rapidity is given by

$$y = \ln\left(\frac{2\omega}{\mathrm{M}}\right), \tag{2.7}$$

where $\sigma_{\gamma/Pb}(y)$ is the cross section of the corresponding photoproduction and $N_{\gamma/\mathrm{Pb}}$ is the photon flux. The terms in the sum represent the incoming nuclei – target and projectile – each acting as a source of the photon. The probability of emitting the photon at mid-rapidity ($y = 0$) is the same for both target and projectile since they are symmetric, see Eq. (2.6).

2.5 Small-x physics

What makes UPC attractive is that it provides a tool to study the evolution of the gluon structure in hadrons. From deeply inelastic experiments (DIS), we know that the collinear gluon distribution grows fast with decreasing x. For exclusive vector meson photoproduction, it is customary to relate $W_{\gamma\mathrm{Pb}}$ to x through

$$x = \frac{\mathrm{M}^2}{W^2_{\gamma\mathrm{Pb}}}. \tag{2.8}$$

The regime where the virtuality $Q^2 > 1$ GeV^2 is treated as DIS regime. This means that the probe (photon) penetrates deeply into the nucleons and 'sees' the internal structure, since x is directly related to the transferred momentum via the centre-of-mass energy s and to the perturbative scale Q^2 as following $s \sim \frac{Q^2}{x}$. Before the LHC era we learned a lot about small-x physics from experiments at HERA in Hamburg. In Fig. 2.5 it is clearly seen that for a fixed scale $Q^2 = 10$ GeV^2 the sea quarks and gluons become dominant in the nucleon with decreasing x (note that the gluon distribution has been scaled down by a factor of 20 [5]).

It is obvious that with increasing energy, we reach smaller x, thus we are able to observe more and more partons in the nucleon. This behaviour cannot continue up to arbitrary high energies, because at some point the area covered by the gluons would be

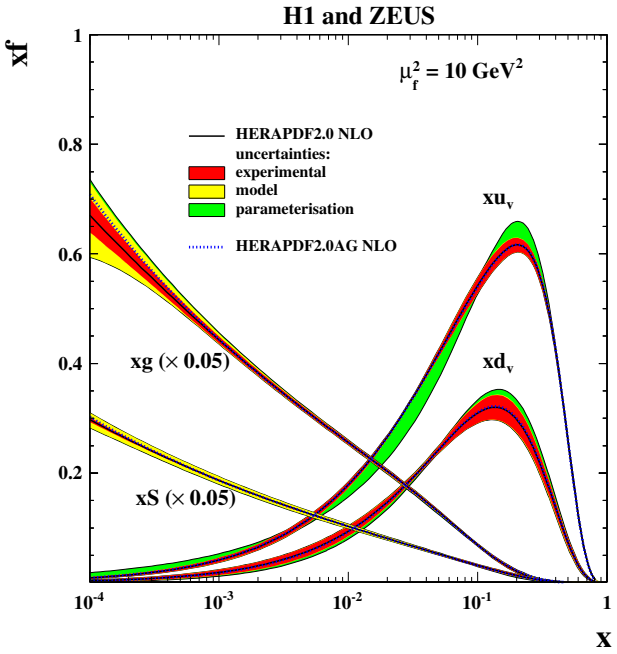

Figure 2.5: Parton distribution functions with decreasing x as extracted by H1 and Zeus from DIS measurements. Taken from [5].

larger than that of the proton. pQCD calculations reveal that this rising of the number of new partons might stop in some moment, when the partons start to recombine. This phenomenon is called *saturation*.

The shape and structure of the nucleons are described by the so-called structure functions. One can suppose that summing all the structure functions of all nucleons in a nucleus one could obtain the structure function of this nucleus. But this assumption has been found experimentally to be wrong. This is quantified by the ratio:

$$R_{F_2}^A(x, Q^2) = \frac{F_2^A(x, Q^2)}{AF_2^{nucleon}(x, Q^2)}, \tag{2.9}$$

where F_2 is the structure function. This ratio seems to be less than 1 in the region where $x < 0.1$. This phenomenon is called *shadowing*, see Fig. 2.6 [6]. There is still the question of what is causing this phenomenon. It could be caused by quarks or by gluons or it might be caused by both of them. This Research Project studies a process especially sensitive to the contribution of gluons to shadowing in Pb nuclei at small x.

Using Eq. (2.5) at mid-rapidity, $y = 0$ and the ψ(2S) mass, for $\sqrt{s_{\rm NN}} = 5.02$ TeV, we can compute the value of $W_{\gamma \rm Pb}$ we are interested in. We obtain $W_{\gamma \rm Pb} = 272$ GeV, which implies, using Eq. (2.8) $x = 1.8 \times 10^{-4}$. So indeed, this process provides a tool to study the gluon distribution of lead nuclei at very small values of x.

In summary, coherent photoproduction of vector mesons in Pb–Pb UPC, is sensitive to the gluon distribution of the target at small x.

To reach small x it is necessary to have colliders which will be able to collide heavy ions at such energies and then detectors, which consequently serve to study these processes. Here, the coherent photoproduction of ψ(2S) is studied with the detector ALICE at the LHC.

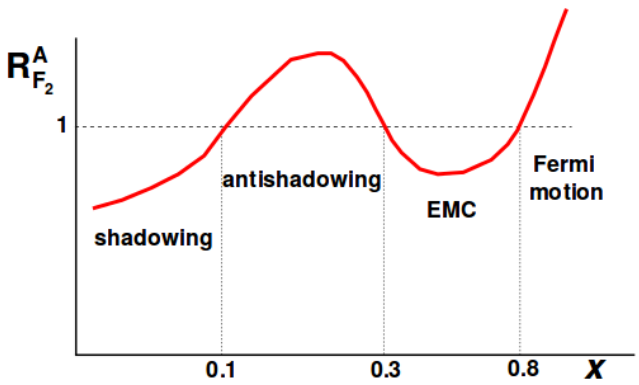

Figure 2.6: The behaviour of the ratio $R^A_{F_2}$ with respect to x at a given Q^2. Taken from [6].

Chapter 3

The ALICE detector

ALICE at the LHC is one of the four main experiments at this accelerator. Its main objective is to study the Quark Gluon Plasma which can be recreated in heavy-ion collisions such as it was shortly after the Big Bang. ALICE was designed to withstand a high particle multiplicity and to measure hadrons, electrons, muons and photons produced in the collisions down to very low transverse momentum $\approx 0.1\text{GeV}/c$.

The detector is composed of two main parts, central barrel and forward muon spectrometer, where the several detector systems are situated. The central barrel is enclosed in the solenoid magnet with a magnetic field of 0.5 T and covers the pseudorapidity of $|\eta| \leq 0.9$ while the forward muon spectrometer has a dipole magnet and provides an integrated field of 3 T·m.

For the purposes of this Research Project the following detectors are needed: Inner Trackig System (ITS), Time Projection Chamber (TPC), Time of Flight (TOF); all located in the central barrel and V0, Zero Degree Calorimeter (ZDC) and Diffractive detector (AD); situated at forward rapidities, see Fig. 3.1. The complete overview of ALICE and of its performance is given in [7] and [8], respectively. In Chap. 4, preliminary results obtained with the muon spectrometer are shown, so a brief description of this detector is also included below.

3.1 Muon spectrometer

The muon spectrometer, placed between 0.9 and 5 metres from the interaction point covering the pseudorapidity $-4 < \eta < -2.5$, contains a front absorber which is made of carbon, concrete and steel. It is composed of five stations consisting of Cathode Pad Chambers. It has two trigger stations, placed behind an iron wall which absorb secondary hadrons and low-momentum muons. The muon trigger has a programmable transverse-momentum threshold and delivers single-muon and dimuon trigger signals. The muon spectrometer is shielded against produced secondary particles by a conical absorber surrounding the beam pipe made of tungsten, lead and steel [10].

3.2 Inner Tracking System

The Inner Tracking System (ITS) is the sub-detector closest to the beam pipe, the place where the collision occur.

It consists of six cylindrical concentric layers, each two layers with different technology, namely from the inner to the outer layer: the silixon pixel detector (SPD), silicon drift detector (SDD) and silicon strip detector (SSD), see Fig. 3.2.

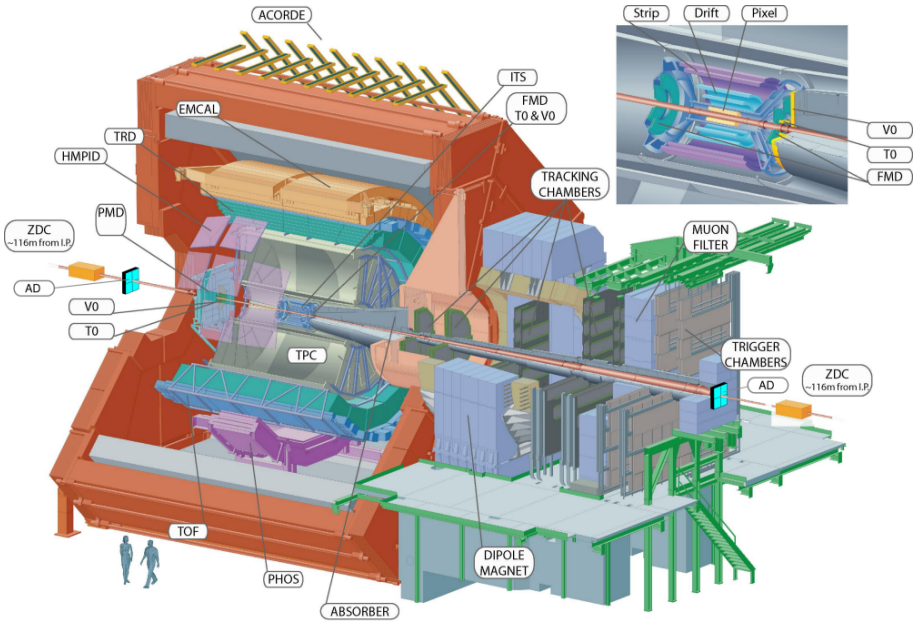

Figure 3.1: Status of the detector in 2012, taken from [9], with the AD detector modules superimposed in blue.

The ITS covers the $|\eta| \leq 0.9$ pseudorapidity range and since it is the closest detector to the beam pipe one of its most important functions is to determine the primary vertex and also secondary vertices caused by decaying short-lived particles. It was estimated that up to 8000 particles per unit rapidity would be present in Pb–Pb collisions, thus it was designed with a minimum of material to prevent possible multiple scattering and to be able to withstand the high-particle-multiplicity environment [11, 12]. ITS serves as a trigger, but it is also used to determine the energy loss of particles and as a stand-alone tracker [13].

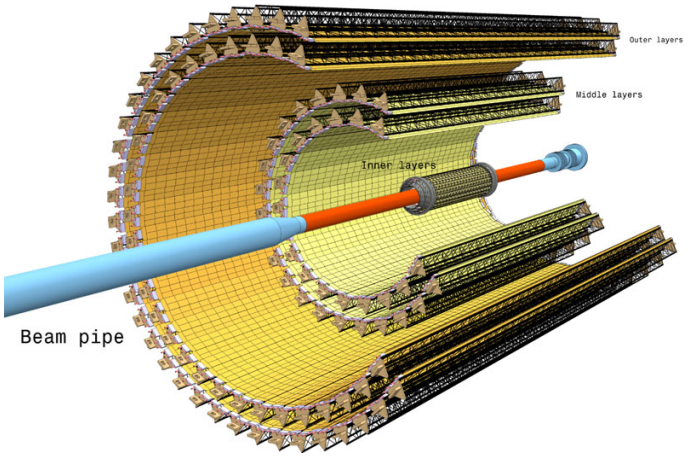

Figure 3.2: Sketch of ITS detector with its 6 layers [14].

3.3 Time Projection Chamber

The Time Projection Chamber (TPC) is a cylindrical detector, surrounding the ITS. It is filled with gas composed of 90 % of $C_2H_2F_4$, 5% of i-C_4H_{10} and of 5% of SF_6 enclosed

in a volume of 90 cm^3. It provides information of the specific energy loss of the particle, and of a particle track. Such as the ITS, the TPC was also constructed aiming at a low budget material, because of the same reasons: to avoid secondary production of particles and multiple scattering [15]. The TPC covers a pseudorapidity region of $|\eta| < 0.9$ and offers particle tracking in a large momentum range $0.1 \leq p_T \leq 100$ GeV/c with a good momentum resolution.

The electric field along the axis of the beam is created by a high-voltage electrode situated at the centre of the TPC. When a particle passes through the TPC, it ionises the gas and produces free electrons. These electrons then drift towards the endcap wire chambers consisting of cathode pads situated at the ends of the TPC, see Fig. 3.3. Each electron ending at the endcap leaves a sample of a track which consequently allows us to fully reconstruct the particle trajectory.

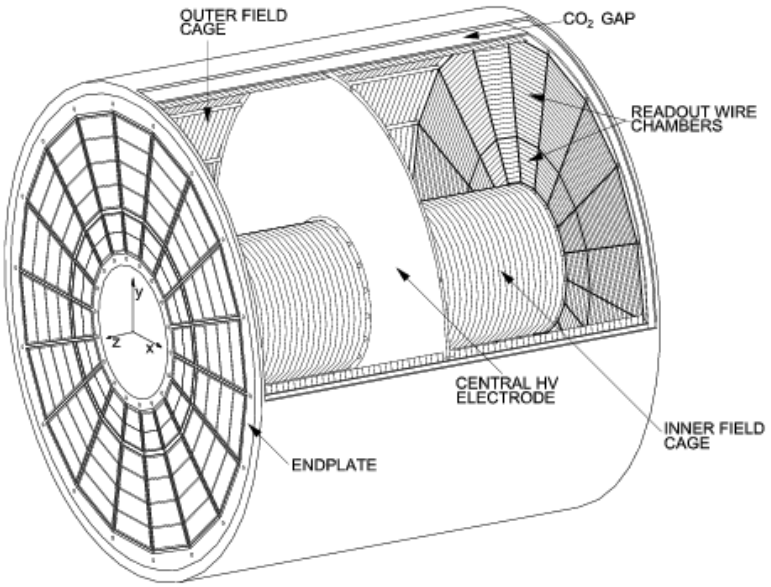

Figure 3.3: Diagram of the TPC. Taken from [16].

3.4 Time of Flight

The Time of Flight (TOF) detector is also a gaseous detector covering the pseudorapidities $|\eta| \leq 0.9$. TOF is used as a trigger for the purposes of the UPC analyses, although the main use of TOF is the identification of charged particles which is provided combining the time of flight of the particle with information on the momentum and track length given by the TPC. TOF is able to identify and separate pions and kaons up to transverse momenta of 2.5 GeV/c and protons up to 4 GeV/c.

The detector consists of 18 segments, the so called supermodules which contain an array of double-stack Multiple-gap Resistive Plate Chamber (MRPC) covering the full azimuthal angle.

3.5 The forward rapidity detectors: V0, ZDC and AD

The arrays of scintillator counters V0A and V0C are able to trigger and separate beam-beam from beam-gas (accelerator background) interactions. Another of its tasks are to

estimate the centrality of the collisions and to measure the luminosity. V0A and V0C are installed in opposite sides along the beam pipe and cover the pseudorapidities $2.8 < \eta < 5.1$ and $-3.7 < \eta < -1.7$, respectively.

Another detector whose purpose is to determine the centrality of the collision is the quartz-spaghetti-fibre calorimeter called Zero-Degree Calorimeter (ZDC). The measurement of the centrality is related to the spectator nucleons which keep the direction along the beam pipe until they hit the ZDC situated at a distance of 112.5 m on either side of interaction point (IP), at zero degrees. ZDC is composed of two calorimeters, each designed to measure neutrons spectators (ZN) or protons spectators (ZP) [15].

The diffractive detector (AD) is another scintillator detector situated at forward rapidities. It consits of 8 scintillator stations divided into 2 groups and each into two layers. One of them is situated on the A side ($z > 0$); the first layer at $z = 1695.17$ cm and second layer at $z = 1698.17$ cm from the IP and covers the pseudorapidity range $4.9 < \eta < 6.3$. The second group of 4 stations is located at $z = -1952.9$ cm and $z = -1955.9$ cm with the wide pseudorapidity coverage of $-6.9 < \eta < -4.9$. The AD detector was added after the Long Shutdown 1 and is in use during Run 2. It improves the acceptance for diffractive systems with masses below 10 GeV/c^2 and also the capability to veto the presence of particles in the AD detector in case of UPC.

Each cell of the AD and V0 detectors can determine the time when a signal arrived. They define time ranges corresponding to arrival times of particles coming from beam-beam (BB) interactions or from beam-gas interactions.

3.6 The ALICE trigger system

Collisions in the LHC occur every 25 ns if the running conditions permit it. In these collisions a large amount of different events are created, however not all are suitable to study a particular branch of physics. These events undergo a process provided by the trigger system, it means in the first place that events are selected according to special requirements of the physics of interest. After passing the selection criteria they are collected and processed. This feature occurs online and it is controlled by the online control system of ALICE. Events are then selected more precisely in the offline framework.

3.6.1 Online control system of ALICE

The Detector Control System (DCS) controls detectors during data taking, checks for possible errors and issues instructions to recover from these failures, thus maximises the efficiency of the data acquisition.

Detectors generating a trigger decision send signals, the so-called inputs, to the Central Trigger Processor (CTP) where they are processed. CTP then ships the processed information through the Local Trigger Unit (LTU) back into the detector. An event signal is then sent to the front-end read-out electronics (FERO) of the detectors. After that the data are injected into Detector Data Links (DDL). Each DDL has on its receiving side the Readout Receiver Card (D-RORC) electronic modules. D-RORC then ships the event fragments into the Local Data Concentrators (LDC) where they are logically assembled into sub-events. Depending on the buffer occupancy of the LDC the Data Acquisition System (DAQ) can decide to enable or disable the most common triggers and send this information to the CTP. After this the sub-events from LDCs are transferred into the event Global Data Collectors (GDC) where thanks to the event-building network are built into the whole event. These events then go into the Permanent Data Storage (PDS). At the same time a copy of the raw data is sent into the High Level Trigger (HLT) which

permits to select interesting events and send them to the LDCs. The diagram of the flow of the data is depicted in the Fig. 3.4.

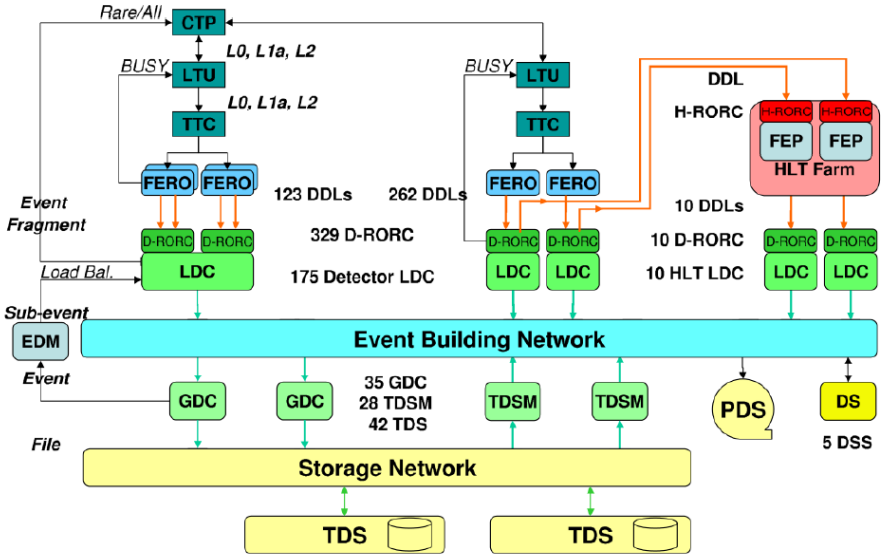

Figure 3.4: The scheme of DAQ. Taken from [7].

Every trigger signal has a different latency, i.e. the time between the moment when a collision occurs till the moment when a signal from the interaction is sent to the trigger system. The inputs with similar latencies form three different levels: 24 inputs for Level 0 (L0), 24 inputs for Level 1 (L1) and 12 inputs for Level 2 (L2) [17]. The function of the levels is to reject unsatisfactory events as soon as possible and thus reduce the dead time of the system.

The L0 Level has the shortest latency, the trigger decision must be made in less than 1.2 μs. The L0 inputs arrive at the detector within 800 ns.

Another fast trigger signal is L1 which arrives at the detector in 6.1 μs after the collision. Both L0 and L1 carry out the first physics selections. An important problem is the contamination of the data sample which may be caused by pile-up effects. To eliminate this problem, for the requested events the signal is controlled in a time window before and after the collision by the past-future protection circuit (p/f) [18].

Although every level checks p/f, the slowest level which waits for p/f is L2. Because of the long drift time the inputs from L2 arrive at the CTP 88.7 μs after the interaction, which gives the necessary time to the CTP to decide about the selection. In this case the decision time is 88 μs.

3.7 Offline Framework - Aliroot

After the online process, the events are selected offline according to the particular physics requirements. To do so it is necessary to have the offline framework, with the following tasks: simulation, reconstruction, detector alignment, calibration, visualisation and analysis of data. Particularly for the ALICE collaboration this framework is called Aliroot.

Chapter 4

Latest results from Run 2

We will present the latest results of J/ψ photoproduction in Pb–Pb at $\sqrt{s_{\mathrm{NN}}} = 5.02$ TeV at both forward and central rapidities with the ALICE detector. These data sets offer larger samples than those used for the Run 1 measurements presented in [19, 20] and reviewed in my B. Sc. thesis. They also offer a larger reach in x due to the almost factor of two increase in $\sqrt{s_{\mathrm{NN}}}$ from Run 1 to Run 2.

4.1 Results at forward rapidities

The data analysis for the period LHC15o and train muon_calo_pass1 was performed with the following trigger classes, see the following Tab. 4.1.

CTEST63-B =	0MSL &	!0UBA &	!0UBC &	!0VBA	- for run 244918
CMUP10-B =	0MSL &	!0UBA &	!0UBC &	!0VBA	- runs 244980-245542
CMUP11-B =	0MUL &	!0UBA &	!0UBC &	!0VBA	- runs 245543-246994
CMUP13-B =	0MUL &	!0UBA &	!0UBC &		- runs 246844-246994

Table 4.1: Trigger classes for the data analysis LHC15o muon_calo_pass1 [21].

where

- 0MSL - low-p_T single muon trigger,
- 0MUL - low p_T unlike-sign dimuon trigger,
- 0VBA - at least one cell in V0A with beam-beam (BB) timing,
- 0UBA - at least one quarter in ADA with beam-beam timing,
- 0UBC - at least one quarter in ADC with beam-beam timing.

The offline global track selection was applied to the candidate events triggered by CMUP10 (CTEST63 and CMUP10 have the same logic), CMUP11 or CMUP13. The ADA and ADC detectors where vetoed to improve the quality of the online trigger. The V0A detector should be empty while the offline decision for the V0C should be either empty or had any activity with timing corresponding to beam-beam events, since the rapidity range of the V0C is smaller than that of the muon spectrometer, thus can occur that muons would miss the V0C, but still be detected in the muon arm. Since in the events we are interested in there are only 2 muons, the next requirement is a maximum of two hits in the V0C. Another requirement is that there should be no tracklets in the SPD, since there is expected no activity in the central region. The next selection criteria is that

exactly two muons detected in the muon spectrometer were required. The pseudorapidity of each muon track was required to be within $-4.0 < \eta_\mu < -2.5$ range. These muon tracks had to have opposite charges. The transverse momentum of the dimuon should be $p_T < 250$ MeV/c. This event sample corresponded to an integrated luminosity of ~ 216 μb^{-1} [21].

The invariant mass spectrum of these dimuons with $p_T < 0.25$ GeV/c is shown in Fig. 4.1 on the left. Since most incoherently produced J/ψ are expected to have momenta larger then 250 MeV/c, a large part of this background is rejected by this selection criterion. The J/ψ and ψ(2S) signals were fitted with Crystal Ball functions. The background is in good agreement with the continuum $\gamma\gamma \to \mu\mu$. The p_T distribution of the J/ψ is shown in Fig. 4.1, right. The distribution was fitted with different Monte Carlo templates produced using the STARLIGHT event generator, and a functional form taken from HERA data on dissociative production. A clear difference can be seen between the p_T of the coherent and the incoherent J/ψ. Other processes taken into account were the J/ψ decaying from the ψ(2S) (feed down) and dissociative J/ψ photoproduction. The cross section of the coherent J/ψ photoproduction at forward rapidities, Fig. 4.2, was compared to different models. The Colour Glass Condensate (CGC) framework using the assumptions by Goncalves, Machado et al. [22, 23] and Lappi and Mantysaari [24] provided good agreement with data but not for all experimental data points. Guzey, Kryshen and Zhalov [25] provided two calculations – based on the EPS09 framework and on the Leading Twist Approximation (LTA). The first one underpredicts the data but remains compatible within the model uncertainties [21]. These are preliminary results from the ALICE Collaboration, which have been originally shown in QM2017 [21]. The analysis towards the final publication is in progress and expected to be concluded during 2018.

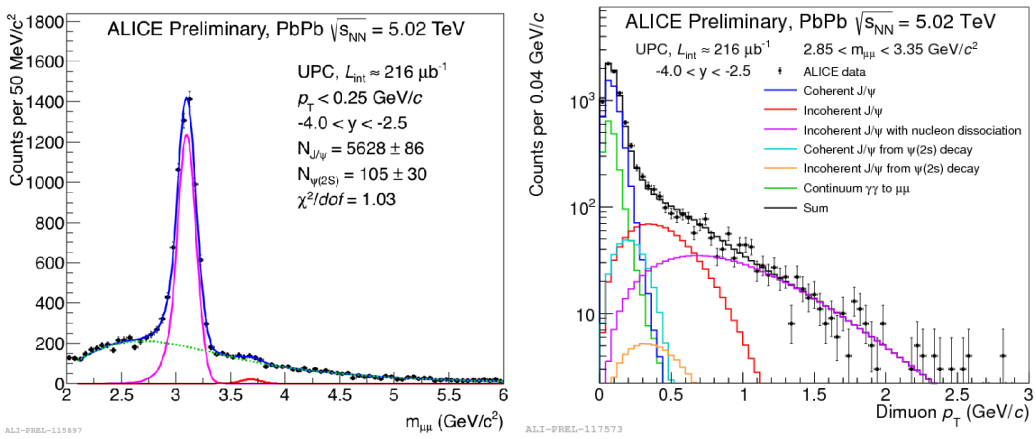

Figure 4.1: (left) The invariant mass spectrum for $\mu^-\mu^+$ pairs with $p_T < 0.25$ GeV/c. (right) Yield of J/ψ as a function of p_T for a mass range around the J/ψ mass, fitted to the sum of contributions from different processes. Taken from [21].

4.2 Results at mid-rapidity

The next study was the analysis of the coherent photoproduction of the J/ψ at mid-rapidity. The integrated luminosity was ~ 95 μb^{-1}. Like in the previous study the central UPC triggers involved vetoes against the activity in the AD detector, V0A and also in the V0C, but in this case there were some topological requirements in the SPD and TOF. During 2017 it was discovered that (i) the reconstruction of the TOF trigger elements was incorrect and (ii) the implementation of the TOF trigger in the simulation of MC events

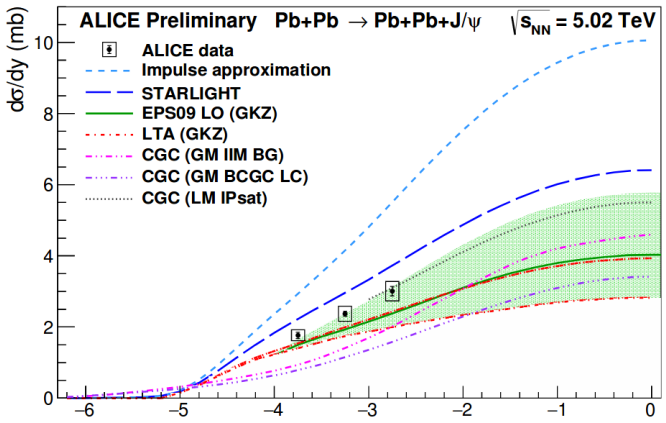

Figure 4.2: The cross section of J/ψ coherent photoproduction in UPC compared with different models. Taken from [21].

also was incorrect. This was discovered during the course of the analysis to measure the coherent J/ψ cross section. After the implementation of corrections, now test data confirm that both problems have been solved. In the next months (end of 2017, beginning of 2018) all events triggered by CCUP8 and CCUP9 will be reprocessed and the MC simulations will be repeated. This is the reason why the following results do not show yet a preliminary cross section. The definition of the CCUP8 and CCUP9 trigger can be found in the Tab. 4.2.

CCUP8 =	!0VBA &	!0VBC &	!0UBA &	!0UBC &	0STP	0OMU
CCUP9 =	!0VBA &	!0VBC &	!0UBA &	!0UBC &	0STP	

0VBA: $\geq$ 1 V0A cell fired in BB timing gate
0VBC: $\geq$ 1 V0C cell fired in BB timing gate
0UBA: $\geq$ 1 ADA cell fired in BB timing gate
0VBC: $\geq$ 1 ADC cell fired in BB timing gate
0STP: $\leq$ 7 outer FO + $\geq$ 2 FO tracklets in η with $|\Delta\Phi| < 150°$
0OMU: 2 $\leq$ TOF maxipads $\leq$ 6 + $\geq$ 2 TOF maxipads with $|\Delta\Phi| < 150°$

Table 4.2: CCUP8 and CCUP9 trigger definitions.

The TPC detector was used for particle identification. Figure 4.3 shows the invariant mass spectrum of $\mu^-\mu^+$ pairs (left) and of e^-e^+ pairs (right). The signals were fitted to Crystal Ball functions. The coherent production of J/ψ was also observed in the decay channel of J/$\psi \to p\bar{p}$. The candidates from this decay channel are shown in Fig. 4.4, left. Another study at mid-rapidity is the analysis of the coherent photoproduction of the ψ(2S) decaying into a J/ψ and two leptons, where the leptons can be either muons or electrons. The observed yield of the $\psi(2S) \to \mu^-\mu^+\pi^-\pi^+$ can be seen on the Fig. 4.4 right. The main contribution of this Research Project is to continue the analysis of the coherent photoproduction of ψ(2S) in UPC at mid-rapidity with the data collected by ALICE in Run 2 during 2015. This is the subject of the next chapter. Note that it is expected that a new set of Pb–Pb data will be collected towards the end of 2018 and the techniques developed here will also be directly applicable to the study of that data set.

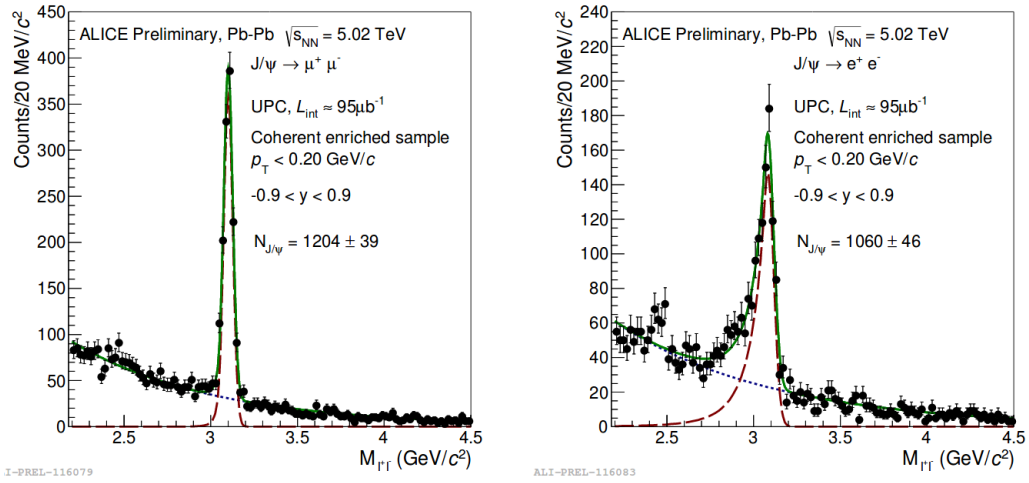

Figure 4.3: The invariant mass spectrum for $\mu^-\mu^+$ pairs (left) and for e^-e^+ pairs (right) fitted by Crystal Ball function. Taken from [21].

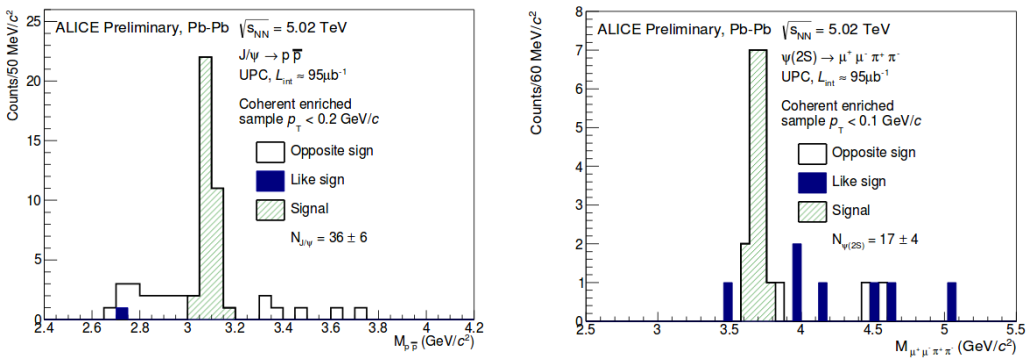

Figure 4.4: The invariant mass spectrum of J/ψ → $p\bar{p}$ (left) and of ψ(2S) → $\mu^-\mu^+\pi^-\pi^+$ (right). Taken from [21].

Chapter 5

Analysis

The analysis of data to measure the $\psi(2S)$ in the different decay channels was done with Pb–Pb collisions at $\sqrt{s_{NN}} = 5.02$ TeV at ALICE for the period LHC15o and Lego train (reconstruction pass): 319. The study of $\psi(2S)$ decaying into 4 tracks and 2 tracks will be discussed in more detail in the following sections.

5.1 Global event selection

The study of the different decay channels of the $\psi(2S)$ was performed at mid-rapidity $|y| < 0.9$ using data collected with the ITS, TPC, V0, AD and ZDC detectors. The original sample contained some 14 million events, and after the train preselection the sample had about 1.3 million events. Some runs were rejected because they did not have the quality standards required for the purposes of this analysis, see Tab. 5.1 for the list of the so-called good runs. Events were further selected if they were triggered by a central barrel trigger the so-called CCUP8-B = *0VBA *0VBC *0UBA *0UBC 0STP 0OMU. The definition of each term can be found in the following:

- * = negation,
- 0VBA = signal in V0A in BB window,
- 0VBC = signal in V0C in BB window,
- 0UBA = signal in ADA in BB window,
- 0UBC = signal in ADC in BB window,
- 0STP = SPD topological trigger; at least two tracks back-to-back in azimuth,
- 0OMU = Between 2 and 6 TOF pads triggered with at least two pads in a back-to-back topology in azimuth.

5.2 AD and V0 decision

From the previous discussion, in the trigger it is already included the decision of the veto against signal in AD and V0 detectors. The illustrative explanation for the necessity of the veto can be simply seen from the Fig. 2.3 and 2.4. On those figures is represented the fact that at mid-rapidity the UPC has only the decay products of the vector meson, in our case of the $\psi(2S)$, which is then measured by the detector. This means, that these events

List of good runs:
244975, 244980, 244982, 244983, 245064, 245066, 245068,
245145, 245146, 245151, 245152, 245231, 245232, 245259,
245343, 245345, 245346, 245347, 245349, 245353, 245396,
245397, 245401, 245407, 245409, 245410, 245411, 245441,
245446, 245450, 245453, 245454, 245496, 245497, 245501,
245504, 245505, 245507, 245535, 245540, 245542, 245543,
245544, 245545, 245554, 245683, 245692, 245700, 245702,
245705, 245738, 245775, 245793, 245829, 245831, 245833,
245923, 245949, 245952, 245954, 246001, 246003, 246012,
246036, 246037, 246042, 246048, 246049, 246052, 246053,
246087, 246089, 246113, 246115, 246151, 246152, 246153,
246178, 246180, 246181, 246182, 246185, 246217, 246222,
246225, 246271, 246272, 246275, 246276, 246424, 246428,
246431, 246434, 246487, 246488, 246493, 246495, 246750,
246751, 246757, 246758, 246759, 246760, 246763, 246765,
246766, 246804, 246805, 246807, 246808, 246809, 246810,
246844, 246845, 246846, 246847, 246851, 246928, 246945,
246948, 246980, 246982, 246984, 246989, 246991, 246994

Table 5.1: Table of good runs.

should not have any other signal at mid-rapidity besides the decay products of the vector meson and no activity at all in the forward rapidity. The correlation of the vetos from the decision of the different detectors can be seen in Fig. 5.1. In the case described above, the figures should be all empty except the area at (0;0), which is of our interest - the empty detector. For the explanation of the meaning of each case, see Tab. 5.2. The activity of the detector is clearly seen in non-required areas. This phenomenon involves the offline repetition of the veto for the activity of the detector. The reason of this feature is that the V0 and AD detectors have a maximum time window of 14 ns. Nevertheless, the charge range during the data taking of the Pb-Pb collisions was larger than this specific time of electronics. The solution to this problem was that the V0 was setup to cover all high charges and thus to miss low charges and then AD was setup in opposite way - covering all low charges and missing high charges. So, the V0 was vetoing only high multiplicity hadronic events and on the other hand the AD was vetoing only low hadronic events. The results of this solution can be seen in the already mentioned Fig. 5.1. After all, this could be corrected offline by adding the selection criteria on the V0 and AD offline decision.

Region	Explication
0-1	Empty V0 and AD detector
1-2	Beam-Beam collision (BB)
2-3	Beam-Gas collision (BG)
3-4	Fake signal - no signal from BB neither BG

Table 5.2: Table with explanation of the meaning of the offline decision area of the V0 and AD detector.

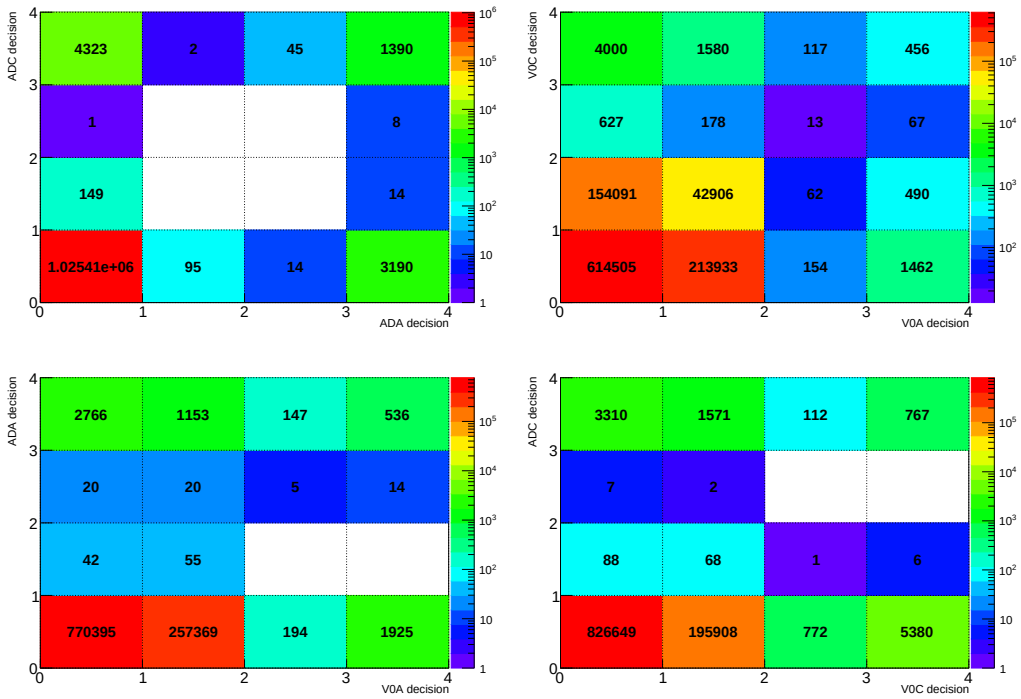

Figure 5.1: The correlation between ADC vs. ADA decision, V0C vs. V0A decision, ADA vs. V0A decision and ADC vs. V0C decision. All decisions are computed using offline information. The numbers correspond to the number of events in each class.

5.3 Selection criteria using the ZDC

After applying the offline veto against activity in AD and V0 we proceed to study the distribution of the ZDC time. Figure 5.2 (upper panels) shows this distribution with the corresponding selection illustrated on the figure by red lines for the ZDCA and the green lines for the ZDCC. The selection for times can be seen perhaps better in Fig. 5.2 (lower panel) showing the correlation between these two times (note the difference in the scale chosen to have better visibility). To reject events from particles in satellite bunches we select the time region (-1,1) ns. When we go back to the upper figures we notice the signal in the region where the time has the value of -999 ns. We also take into account this region since -999 ns is an arbitrary time assigned to events without activity.

As was mentioned in Chap. 2, independent photon interactions may cause the emission of neutrons which are detected in the ZDC detector. In the case of the coherent photoproduction, we accept up to 6 emitted neutrons of total energy $\approx$ 15 TeV. This energy must be recorded in the ZDC time window (-1,1) ns. Thus another selection criteria is to request the ZDC energy to be less than 15 TeV in both sides and can be seen in the Fig. 5.3.

5.4 Selection criteria related to the interaction vertex

Figure 5.4 shows the SPD vertex contributors already after the requirement of having at least one of them. On the right hand side of the same figure we can see the study of the distance between SPD vertex in the z direction - the direction of the beam, and primary vertex (PV) also in the z-axis to ensure that events became from the same vertex. The cut on the plot, the green lines, illustrates the region we are interested in. The signal

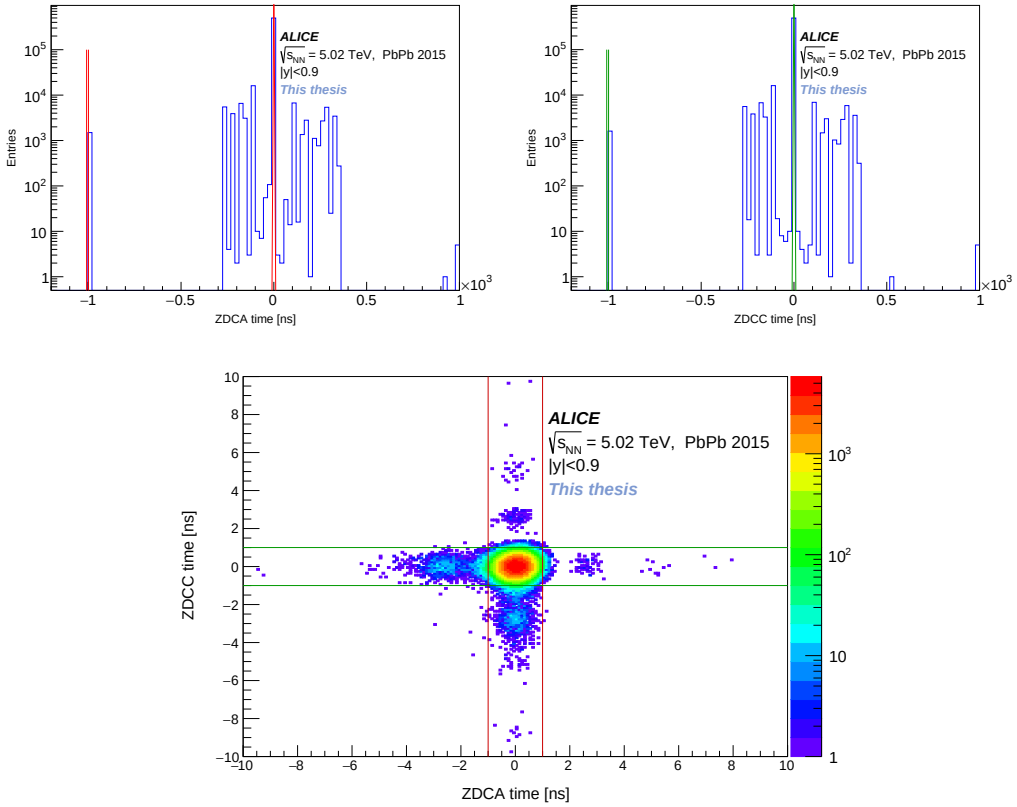

Figure 5.2: The illustrated cut by red and green lines for ZDCA and ZDCC time, respectively. This selection criterion is listed in Tab. 5.3 as 5c) and 5d).

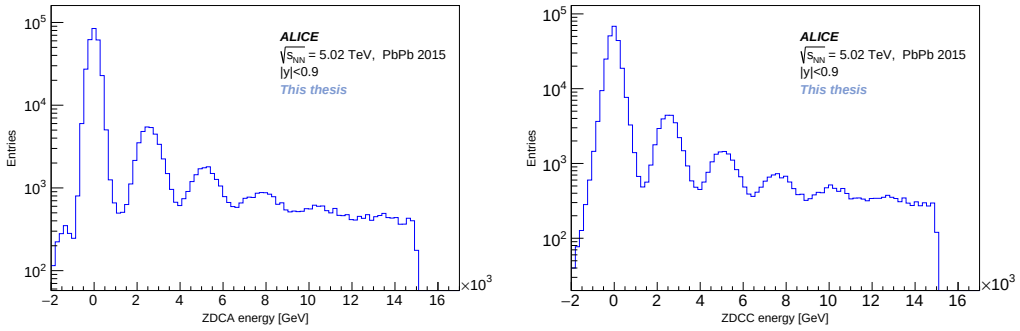

Figure 5.3: The ZDC energy cut below 15 TeV corresponding to the energy of 6 neutrons. This selection criterion is listed in Tab. 5.3 as 5a) and 5b).

exceeding the region of -0.3 cm and +0.3 cm is the background coming from the soft electron-positron pairs created by the strong electromagnetic fields of the incoming nuclei.

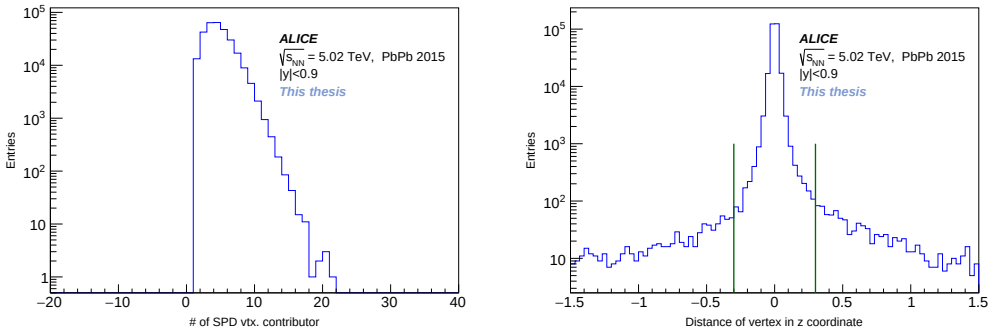

Figure 5.4: The cut for at least 1 SPD vertex contributor (left) and the illustration of the cut of the distance between SPD vertex and the primary vertex. This selection criterion is listed in Tab. 5.3 as 6 and 7.

5.5 The selection of tracks

After these selection criteria we want to be sure that the tracks which we are working with are 'good'. The definition of what is 'good' in our case is the following:

- The track must exist.
- Application of Filter Bit 0 (Filter Bit 4 for two tracks analysis); Standard TPC only track cuts.
- 70 TPC clusters as minimum.
- The $\chi^2 < 4$ per TPC cluster.
- The distance of closest approach DCA_z in z direction is less than 2 cm and DCA_{xy} is p_T dependent. For four tracks analysis is $|\mathrm{DCA_{xy}}| < 4(0.0182 + 0.0350/\mathrm{p_T^{1.01}})$ ($|\mathrm{DCA_{xy}}| < (0.0182 + 0.0350/\mathrm{p_T^{1.01}})$ for 2 tracks analysis).
- Set DCA to vertex 2D.
- TPC and ITS refit.
- At least one hit in SPD.

As was already mentioned the final state of the photoproduction is only the vector meson, i.e. in the detector are only the decay products of the mother particle. This implies another important requirement, the requisite of having exactly four (two) tracks. The paired particles have to have the opposite charges, so the sum of all of them must be zero. We said in a previous chapter that the vector meson is created with very small p_T. When we analyse this statement, it implies that in the case of the decay channel $\psi(2\mathrm{S}) \to \pi^-\pi^+\mathrm{J}/\psi$, where $\mathrm{J}/\psi \to l^+l^-$, the J/ψ decays almost at rest and the pions take small p_T with them. Thus the p_T of the leptons (μs or electrons) will be greater than that of the pions. This kinematic fact, is reflected in the selection criterion for lepton tracks: $p_T(l^\pm) > 1.1$ GeV/c. The same assumption is valid for the direct decay channels

$\psi(2S) \to l^- l^+$ but with slightly different cut $p_T(l^\pm) > 1.0$ GeV/c where at least one track has to fulfil this criterion.

To distinguish the muons and electrons from each other we use the TPC particle identification (PID) by their energy loss dE/dx. We suppose that muons (electrons) are within 4σ (3σ for 2 tracks decay) of the muon (electron) PID hypothesis, where σ means the resolution of the measurement of the dE/dx at a given particle momentum. The energy loss of muons (electrons) for the 4-tracks decay channel before and after the cut for nσ can be seen in Fig. 5.5. The energy loss of dielectron and dimuon pairs coming from the direct decay channel of $\psi(2S)$ are shown in the same figure after the PID cut. The line depicted in this figure is just an alternate cut which serves as an uncertainty estimation of this selection.

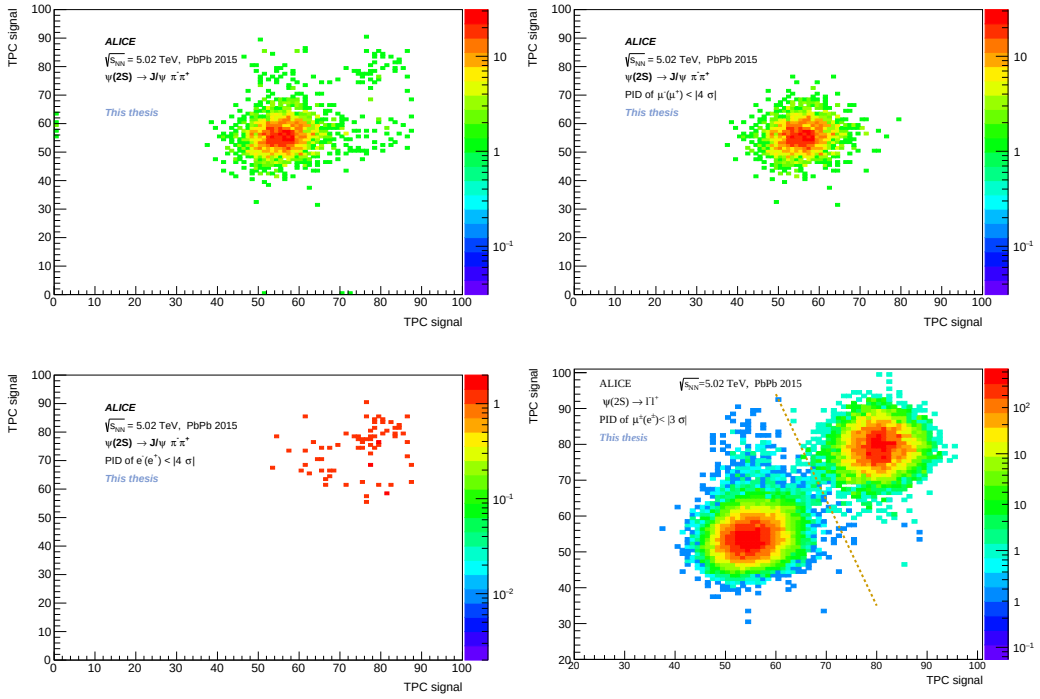

Figure 5.5: (upper panels) On the left hand side there is energy loss dE/dx of positive charged tracks vs negatively charged tracks before the cut for PID. On the right hand side there is the energy loss dE/dx of muons after the PID cut. (lower panels) The dE/dx of the electrons vs. positrons after the PID cut is on the left. On the right hand side there is dE/dx of muons and electrons coming from the direct decay channel. The energy loss after the cut for the PID for particular particle is depicted in the same figure. The line is an alternate cut for an uncertainty estimation of the selection. The cut for 4 particle decay channel can be seen in Tab. 5.3 as cut 13) and direct decay channel in Tab. 5.4 as 12).

5.6 The invariant mass of $\psi(2S) \to J/\psi\pi^-\pi^+$, $J/\psi \to l^- l^+$

After the application of all the selection criteria for tracks we use TLorentzVector to build the J/ψ candidate and to to plot the distribution of the invariant mass of the muon (electron) pair against its transverse momenta p_T. Then we restrict the mass of muon (electron) pair to be compatible with the mass of the J/ψ. So the cut for muon (electron) pair goes from 3.0 GeV/c^2 to 3.2 GeV/c^2 (2.7 GeV/c^2 to 3.2 GeV/c^2). After that we add

the four momentum of the pion pair and we obtain the invariant mass of the ψ(2S). The distribution of the invariant mass of the ψ(2S) (before the restriction of its invariant mass) against its p_T can be seen in Fig. 5.6.

Then we select the cut for the invariant mass of the ψ(2S) to be in the range of (3.6,3.8) GeV/c^2 for muons and (3.3,3.8) GeV/c^2 for electrons. The plot of this selection against its p_T is depicted in Fig. 5.7.

Since this analysis is the study of the coherent VM photoproduction, i.e. the vector meson is created almost at the rest (p_T of few tens of MeV), we apply the cut for the transverse momentum of the ψ(2S) to be < 0.2 GeV/c, see Fig. 5.8.

All these selection criteria are summarised in Tab. 5.3 for $\psi(2S) \to J/\psi\pi^-\pi^+$, $J/\psi \to \mu^-\mu^+$ and in Tab. 5.4 for the $\psi(2S) \to J/\psi\pi^-\pi^+$, $J/\psi \to e^-e^+$ decay channel.

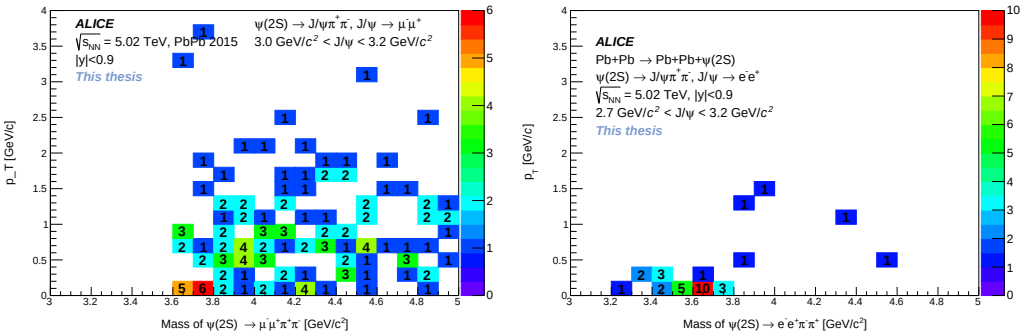

Figure 5.6: The mass of ψ(2S) vs. its p_T for the decay channel $\psi(2S) \to \mu^+\mu^-\pi^+\pi^-$ (left) and the same for the decay channel $\psi(2S) \to e^+e^-\pi^+\pi^-$ (right) after the cut for the mass of the J/ψ candidate. The cut can be seen in Tab. 5.3.

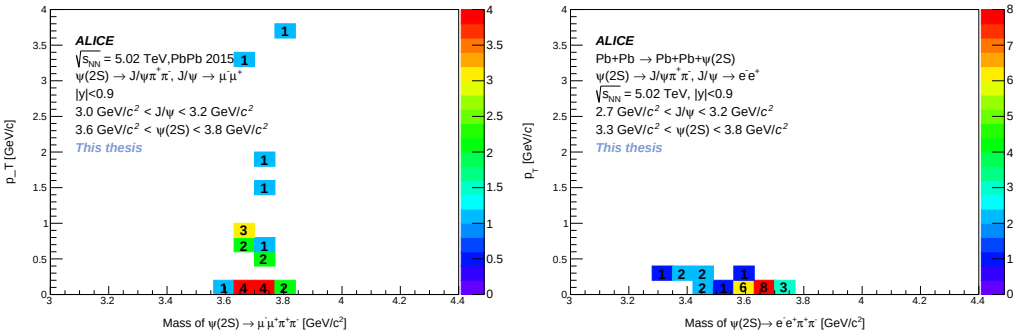

Figure 5.7: The cut for the mass of the ψ(2S) candidate vs. its p_T for the decay channel $\psi(2S) \to \mu^+\mu^-\pi^+\pi^-$ (left) and the same for the decay channel $\psi(2S) \to e^+e^-\pi^+\pi^-$ (right). The cut can be seen in Tab. 5.3.

5.7 The invariant mass of $\psi(2S) \to l^-l^+$

The ψ(2S) also decays directly into two leptons (muons or electrons). However the muon pairs not only come from the decay of the ψ(2S), they are mainly a result of the $\gamma\gamma \to \mu^-\mu^+$ reaction.

The selection criteria were described in the previous section with some slight modifications which were also already mentioned above.

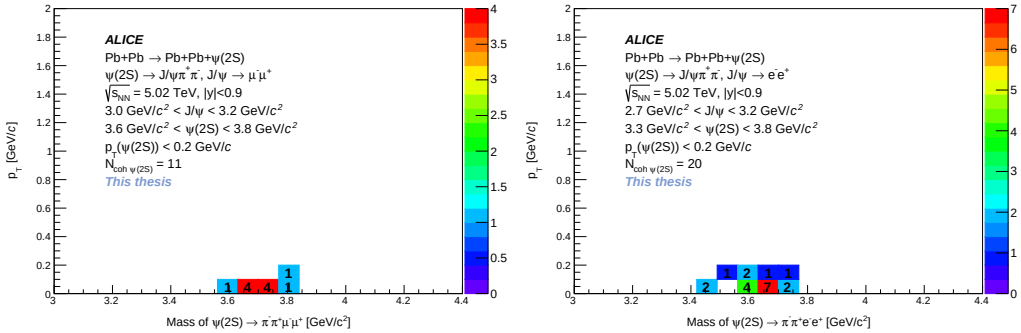

Figure 5.8: Candidates for coherently produced ψ(2S) vs their p_T from the decay channel $\psi(2S) \rightarrow \mu^+\mu^-\pi^+\pi^-$ (left) and the same for the decay channel $\psi(2S) \rightarrow e^+e^-\pi^+\pi^-$ (right). The cut can be seen in Tab. 5.3.

		$l^-l^+ = \mu^-\mu^+$	$l^-l^+ = e^-e^+$
Marker	Cut	Selected events	Selected events
	Analysed triggers	1.434254 $\times 10^7$	1.434254 $\times 10^7$
	'Train' preselection	1.32063 $\times 10^6$	1.32063 $\times 10^6$
1	Bad runs rejected	1045856	1045856
2	CCUP8	949192	949192
3a	ADA empty	944956	944956
3b	ADC empty	940871	940871
4a	V0A empty	703784	703784
4b	V0C empty	560265	560265
5a	|ZDCAtime| < 1 ns or ZDCAtime = -999 ns	496232	496232
5b	|ZDCCtime| < 1 ns or ZDCCtime = -999 ns	441564	441564
5c	ZDCA energy < 15 TeV in (-1,1) ns	353532	353532
5d	ZDCC energy < 15 TeV in (-1,1) ns	295700	295700
6	At least 1 contributor to the vertex	295696	295696
7	|SPD vtx. - primary vtx.| < 0.3 cm	290822	290822
8	Exactly 4 tracks	290822	290822
9	Opposite charges of 4 tracks	165864	165864
10a	track 1 is Good Track	159562	159562
10b	track 2 is Good Track	157310	157310
10c	track 3 is Good Track	155464	155464
10d	track 4 is Good Track	151696	151696
11	p_T $l^+ > 1.1$ Gev	13078	13078
12	p_T $l^- > 1.1$ Gev	2806	2806
13	PID TPC of lepton pair	2642	71
14	PID TPC of pion pair	2310	60
15	Cut for mass of J/ψ	166	34
16	Cut mass ψ(2S)	23	26
17	Cut for $p_T < 0.2$ GeV/c of ψ(2S)	11	20

Table 5.3: Table of used cuts for extraction of the signal of ψ(2S) from decay channel $\psi(2S) \rightarrow \pi^+\pi^-$J/$\psi$, where J/$\psi \rightarrow l^-l^+$, where l^-l^+ are eithere muons or electrons.

Marker	Cut	$l^-l^+ = \mu^-\mu^+$ Selected events	$l^-l^+ = e^-e^+$ Selected events
	Analysed triggers	1.434254 $\times 10^7$	1.434254 $\times 10^7$
	'Train' preselection	2.48379 $\times 10^6$	2.48379 $\times 10^6$
1	Bad runs rejected	1930416	1930416
2	CCUP8	1630626	1630626
3a	V0A empty	1297321	1297321
3b	V0C empty	1108496	1108496
4a	ADA empty	1104539	1104539
4b	ADC empty	1101261	1101261
5a	|ZDCAtime| < 1 ns or ZDCAtime = -999 ns	963215	963215
5b	|ZDCCtime| < 1 ns or ZDCCtime = -999 ns	847925	847925
5c	ZDCA energy < 15 TeV in (-1,1) ns	630830	630830
5d	ZDCC energy < 15 TeV in (-1,1) ns	630830	630830
6	At least 1 contributor to the vertex	630756	630756
7	|SPD vtx. - primary vtx.| < 0.3 cm	601057	601057
8	Exactly 2 tracks	601057	601057
9a	track 1 is Good Track	576638	576638
9b	track 2 is Good Track	558704	558704
10	Opposite charges of 4 tracks	408858	408858
11	p_T l^+ or l^- > 1.1 Gev	36833	36833
12	PID TPC of lepton pair	25933	6800
13	Cut for mass of ψ(2S)	212	138
14	Cut for $p_T < 0.2$ GeV/c of $\psi(2S) \to l^-l^+$	145	97

Table 5.4: Table of used cuts for extraction of the signal of ψ(2S) from direct decay channel $\psi(2S) \to l^-l^+$.

Figures 5.9 and 5.10 show the invariant mass of the muon and electron pairs, respectively. The figures also show the regions selected for the analysis. This region (3.6;3.8) Gev/c^2 is represented with the green lines. After this, we applied the cut for the coherence of the ψ(2S) which means, that the transverse momentum of the dilepton pair has to be $p_T \leq 200$ MeV/c, see Fig. 5.11 for $\mu^-\mu^+$ pairs (see Fig. 5.12 for e^-e^+ pairs). These candidates are for both ψ(2S) and $\gamma\gamma \to \mu^-\mu^+$, and the second option is the main contribution.

Thus we obtained after all 145 (97) candidates for these two processes in the muon (electron) channel.

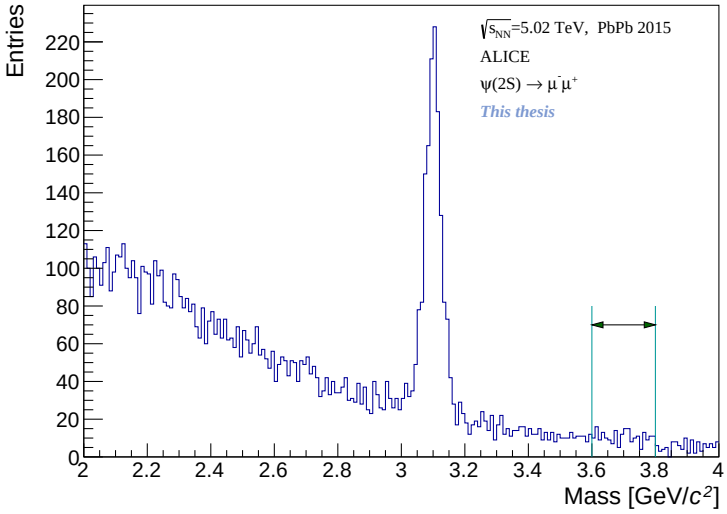

Figure 5.9: The invariant mass of muon pairs. Green lines represent the cut for the invariant mass of the ψ(2S).

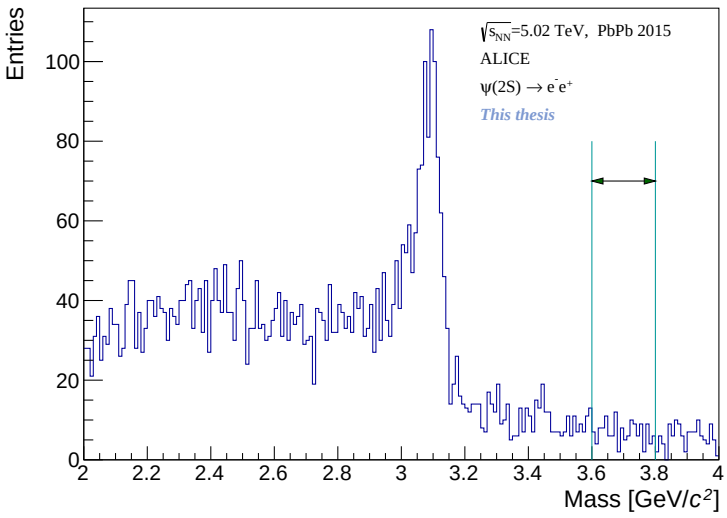

Figure 5.10: The invariant mass of electron pairs. Green lines represent the cut for the invariant mass of the ψ(2S).

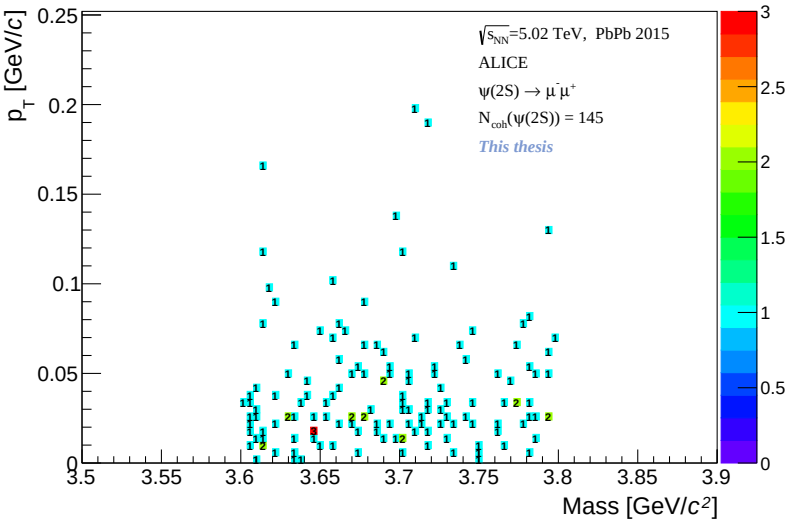

Figure 5.11: The coherent ψ(2S) candidates from the direct decay channel $\psi(2S) \rightarrow \mu^-\mu^+$. The cut can be seen in 5.4 as 14.

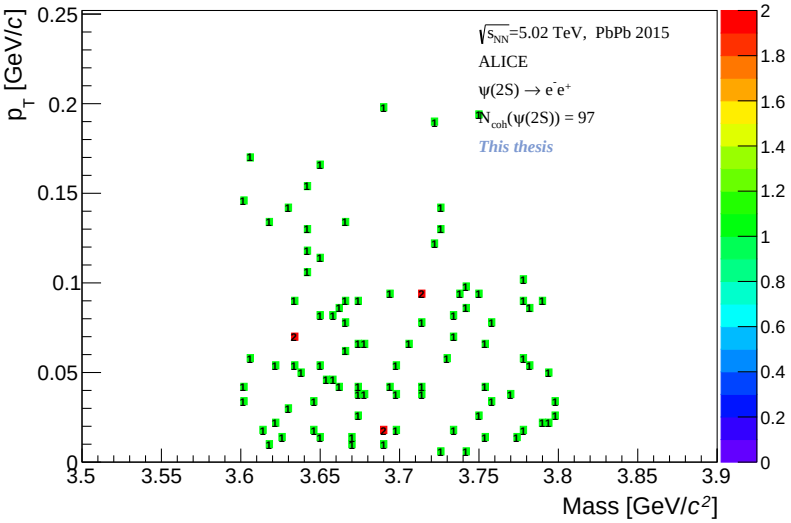

Figure 5.12: The coherent ψ(2S) candidates from the direct decay channel $\psi(2S) \rightarrow e^-e^+$. The cut can be seen in 5.4 as 14.

5.8 Monte Carlo simulations for the coherent photoproduction of the $\psi(2S)$

To be sure that our methods were done correctly we study the photoproduction of $\psi(2S)$ in Monte Carlo simulations (MC) since there are available event samples with larger statistics. Our MC data are either data of reconstructed particles or the generated particles. The latter one are the simulations of the collisions. These collisions are then folded with the full detector simulation = reconstructed particles. Since the detector is not perfectly efficient, there is good reason to study the processes of our interest in MC simulations.

We used the same cuts for the reconstructed particles as for the real data, see Tab. 5.3 and 5.4. In Fig. 5.13 we can see the transvere momenta of leptons and pions decaying from $\psi(2S)$ through the decay channel $\psi(2S) \to J/\psi\pi^-\pi^+$. As was mentioned above, the $\psi(2S)$ has very small momentum, the mass difference between $\psi(2S)$ and J/ψ +pions is small, then J/ψ and pions have small momentum. This is nicely demonstrated in the Fig. 5.13 for particles with positive charge. The same result we would obtain for the negatively charged particles.

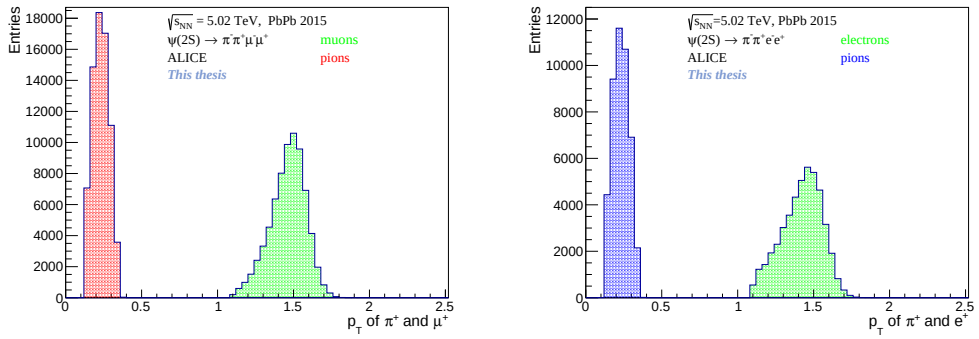

Figure 5.13: (left) Reconstructed transverse momentum of π^+ and μ^+ from Monte Carlo simulations. (right) p_T of π^+ and e^+ from Monte Carlo simulations.

To identify the decaying particles with small p_T we use particle identification from the TPC. Muons and electrons have the specific ionisation loss $\mathrm{d}E/\mathrm{d}x$ in the TPC. On the left hand side up and down in the Fig. 5.14 there can be seen the $\mathrm{d}E/\mathrm{d}x$ of muons and electrons, respectively, after applying the cut for PID, see Tab. 5.3 cut 13 and 14. As in the previous section, we again used the following equation:

$$\sigma_{l_1}^2 + \sigma_{l_2}^2 < 4^2, \tag{5.1}$$

where l_1 and l_2 are the tracks of the leptons. The σs are again the mean-square deviations from the Bethe-Bloch expectation in the TPC. On the right hand side in Fig. 5.14 are depicted the tracks after the cut for PID to be within 4σ. This is shown for the direct decay channel on the Fig. 5.15, where muons and electrons where required to be within 3σ.

After this we have prepared everything to see distributions of the mass, rapidity and p_T of the lepton pairs. After applying cuts from Tab. 5.3 we obtained the distributions of the J/ψ, its p_T and rapidity y. These distributions are shown in Fig. 5.16 for the decay channel $\psi(2S) \to J/\psi\pi^-\pi^+$, where $J/\psi \to \mu^-\mu^+$. In the case where the J/ψ decays into electrons, these distributions are shown in Fig. 5.17. After that, applying criteria 16 and 17 from the same table, we finally obtain the distribution of the mass, p_T and rapidity of the $\psi(2S)$.

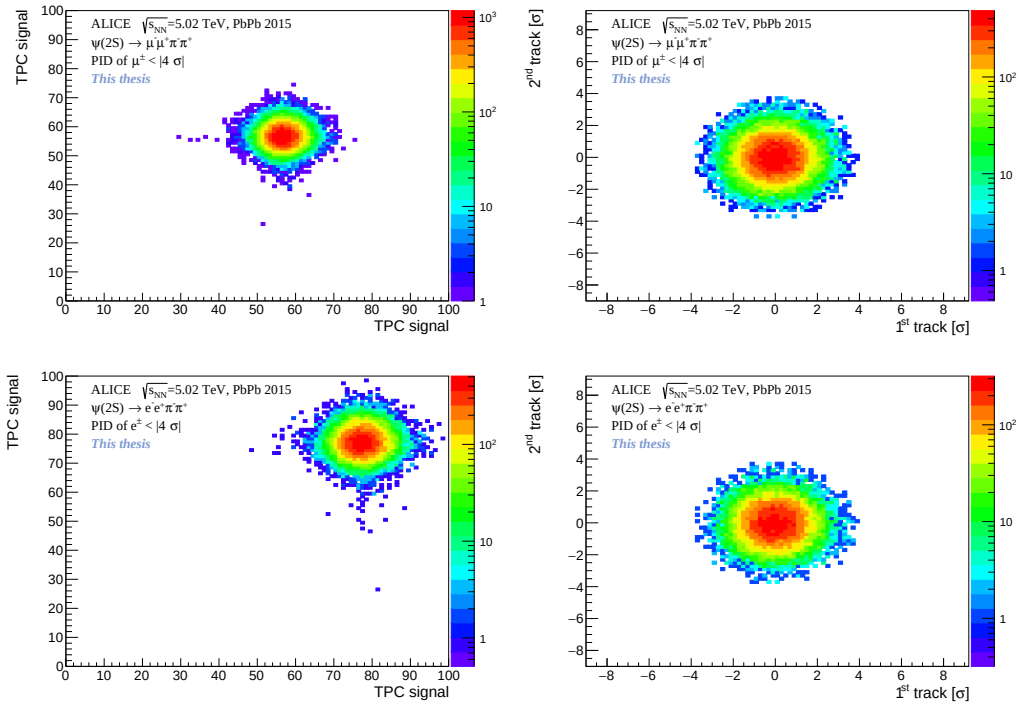

Figure 5.14: $\mathrm{d}E/\mathrm{d}x$ and PID for the 4-track decay of the ψ(2S): (upper panels) On the left hand side there is energy loss $\mathrm{d}E/\mathrm{d}x$ of muons after the PID cut and on the right hand-side is depicted the PID of muons after this cut from Monte Carlo simulation. (lower panels) On the left hand side there is $\mathrm{d}E/\mathrm{d}x$ of electrons after the PID cut and on the right hand-side is depicted the PID of electrons after this cut from Monte Carlo simulation.

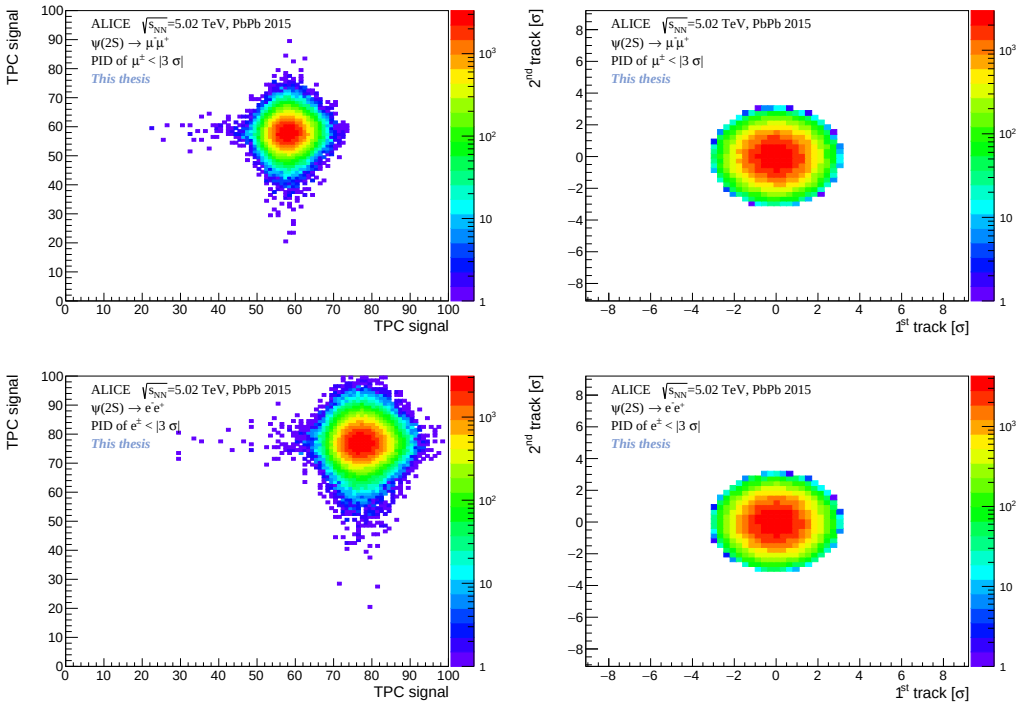

Figure 5.15: $\mathrm{d}E/\mathrm{d}x$ and PID for the direct decay of the ψ(2S): (upper panels) On the left hand side there is energy loss $\mathrm{d}E/\mathrm{d}x$ of muons after the PID cut and on the right hand-side is depicted the PID of muons after this cut from Monte Carlo simulation. (lower panels) On the left hand side there is $\mathrm{d}E/\mathrm{d}x$ of electrons after the PID cut and on the right hand-side is depicted the PID of electrons after this cut from Monte Carlo simulation.

We do the same for the direct decay channel, see Figs. 5.18 and 5.19. Applying criteria 13 and 14 from Tab. 5.4 we get as a result the invariant mass of the $\psi(2S)$, its p_T and rapidity (see the same figures).

For the generated particles we just sum the four-momenta of the decay product of the $\psi(2S)$ according to the decay channel, see Fig. 5.20 and using the TLorentzVector we plot the distribution of the $\psi(2S)$ to ensure that all was done all right, see the same figure.

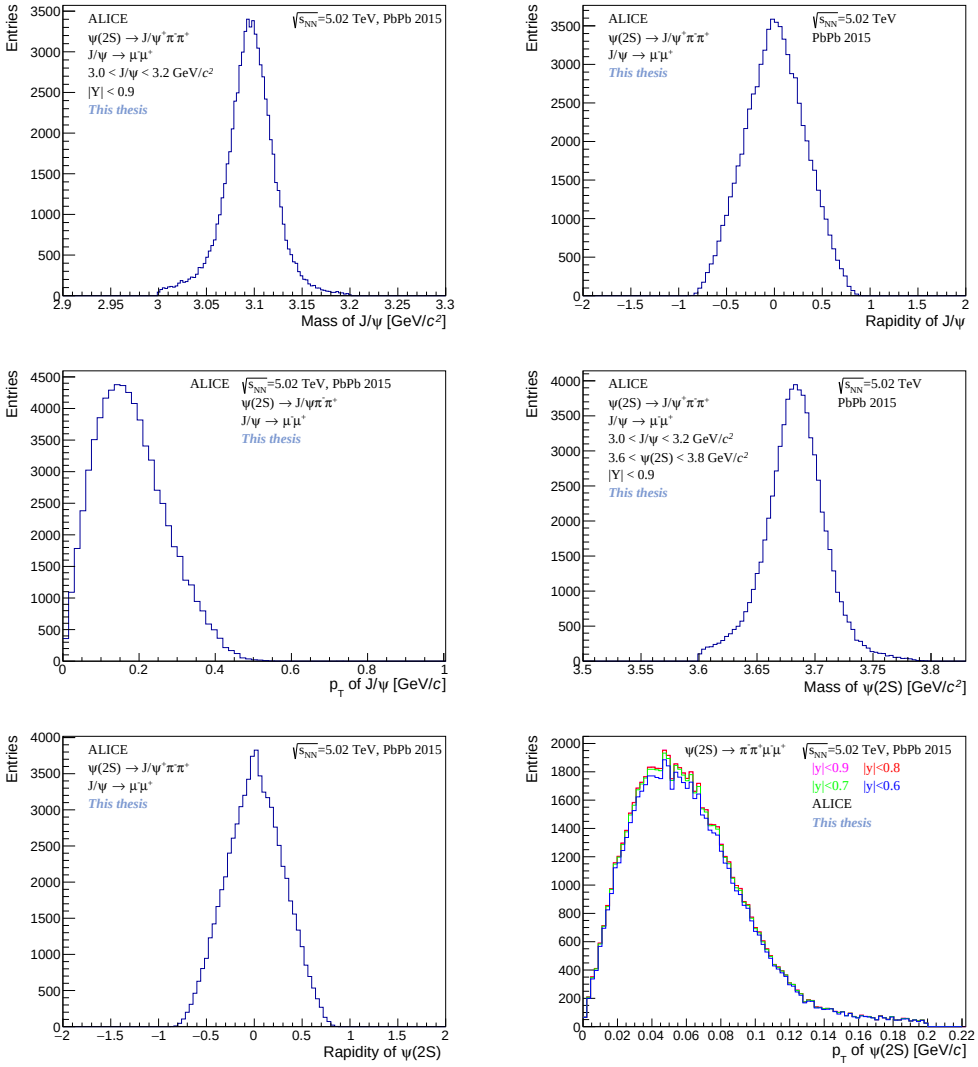

Figure 5.16: (upper panels) Reconstructed mass of the J/ψ from the decay channel $\psi(2S) \to \mu^-\mu^+\pi^-\pi^+$, its transverse momentum p_T and rapidity y from Monte Carlo simulation. (lower panels) Reconstructed mass of the $\psi(2S)$ its transverse momentum p_T and rapidity y from Monte Carlo simulation.

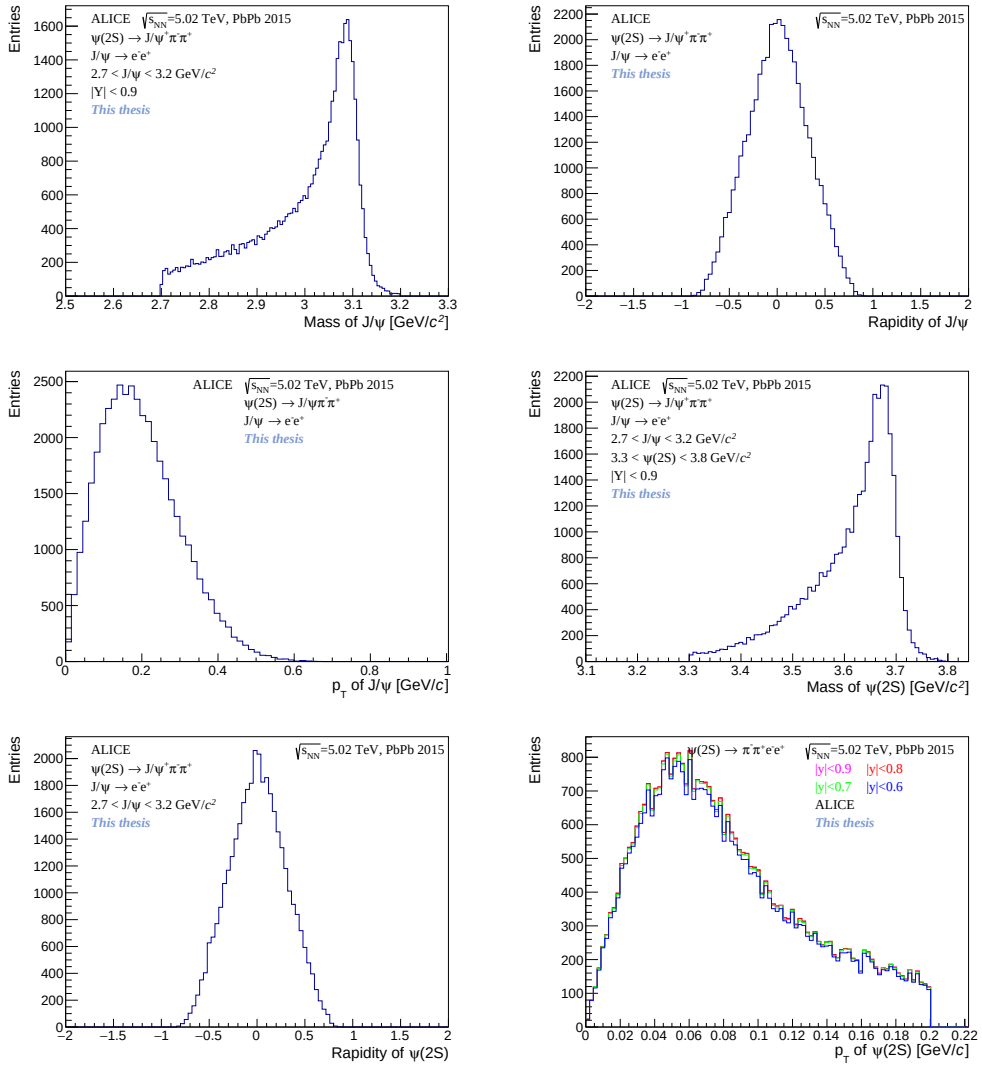

Figure 5.17: (upper panels) Reconstructed mass of the J/ψ from the decay channel $\psi(2S) \rightarrow e^-e^+\pi^-\pi^+$, its transverse momentum p_T and rapidity y from Monte Carlo simulation. (lower panels) Reconstructed mass of the $\psi(2S)$ its transverse momentum p_T and rapidity y from Monte Carlo simulation.

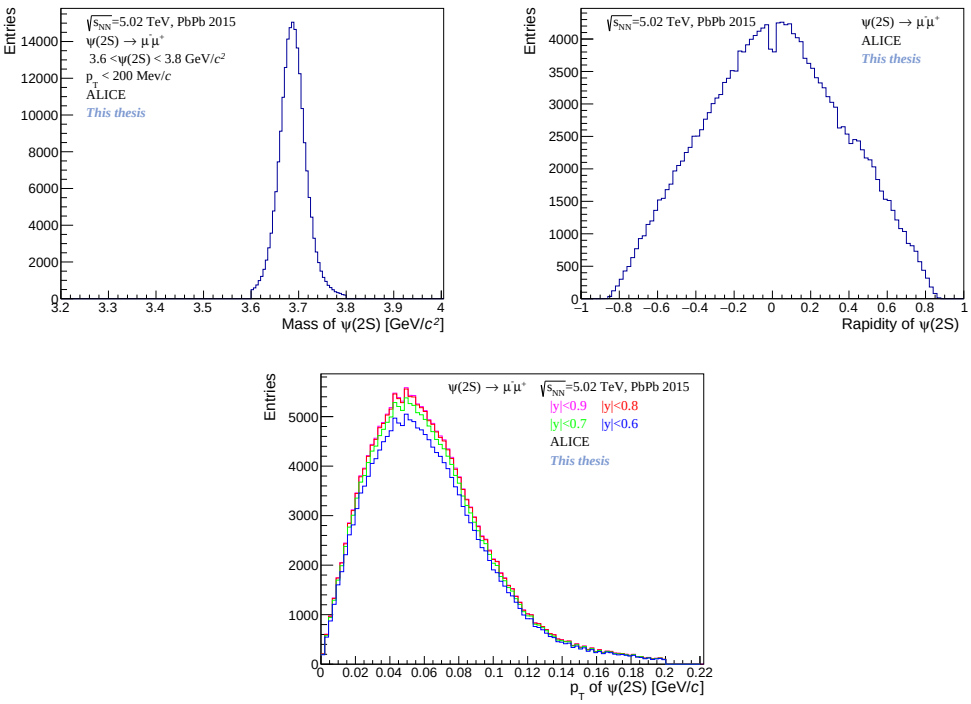

Figure 5.18: (upper panels) Reconstructed mass of the $\psi(2S) \to \mu^-\mu^+$ and rapidity y from Monte Carlo simulation. (lower panel) Reconstructed transverse momentum p_T of $\psi(2S)$ from Monte Carlo simulation.

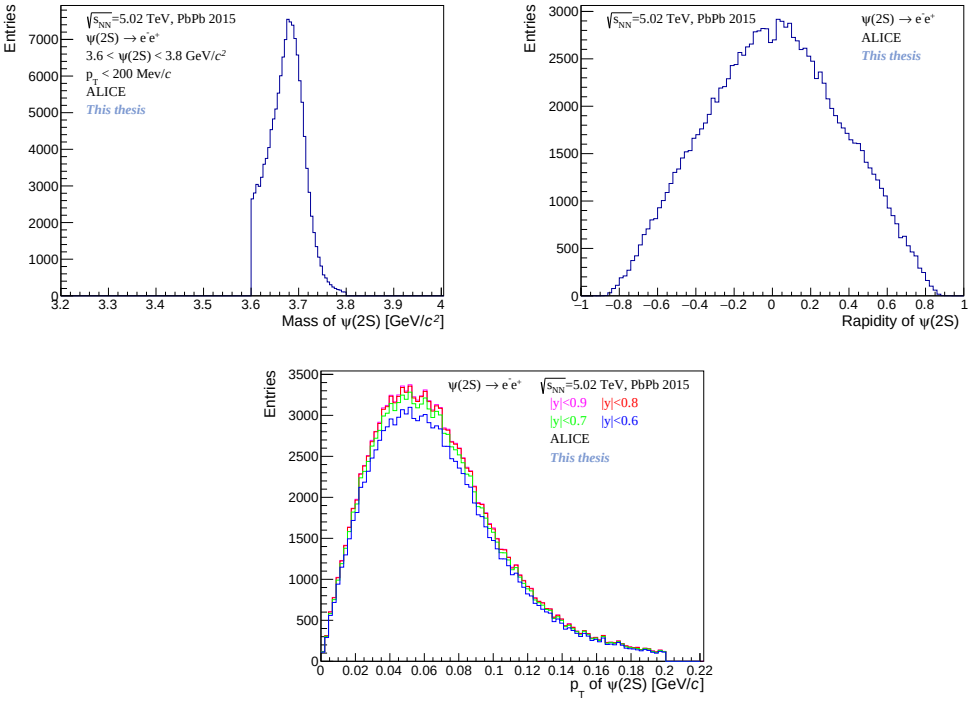

Figure 5.19: (upper panels) Reconstructed mass of the $\psi(2S) \to e^-e^+$ and rapidity y from Monte Carlo simulation. (lower panel) Reconstructed transverse momentum p_T of $\psi(2S)$ from Monte Carlo simulation.

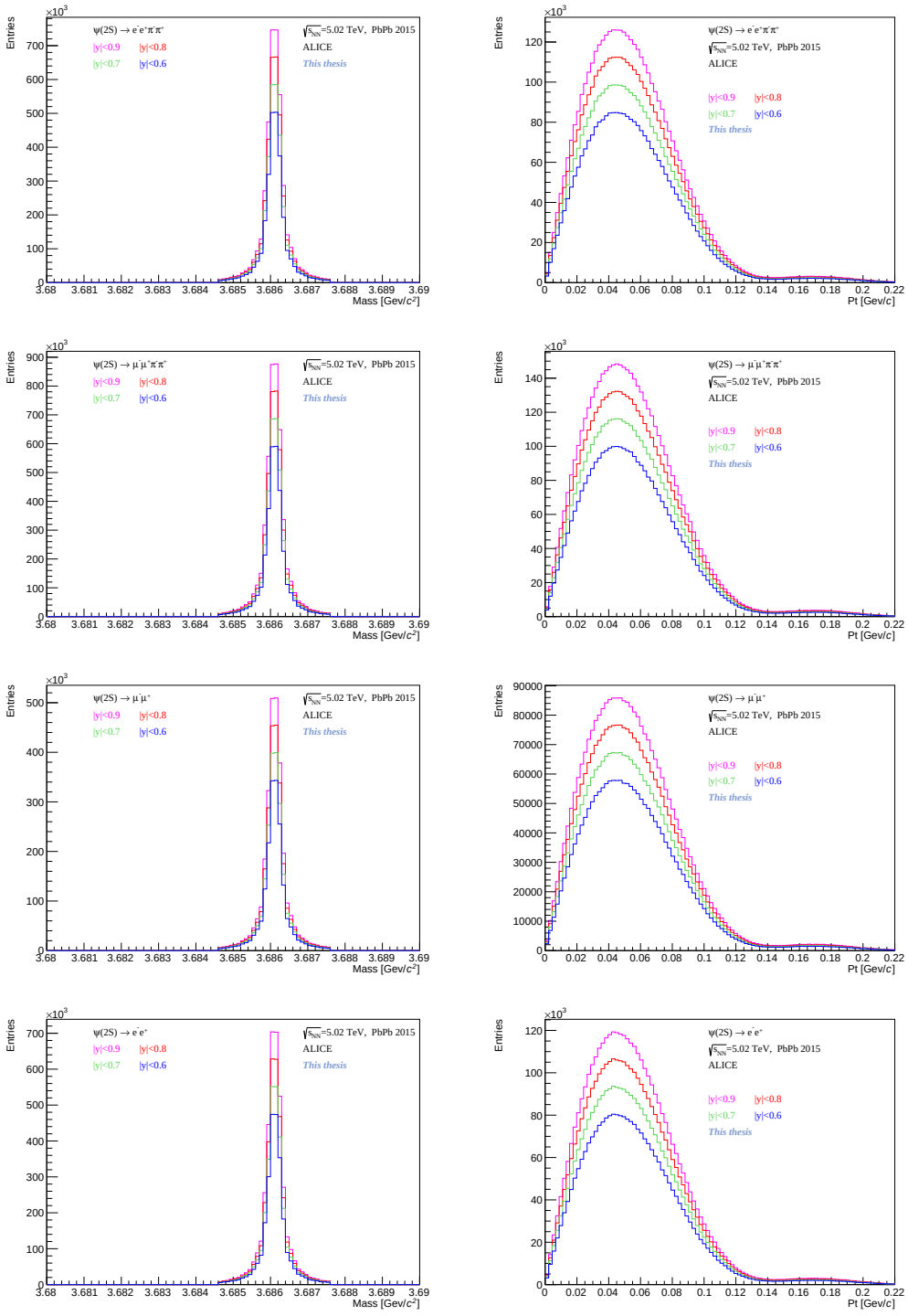

Figure 5.20: The generated invariant mass of the ψ(2S) according to particular decay channel (left) and its transverse momentum p_T (right) from Monte Carlo simulation.

5.9 The study of the efficiency and acceptance

Thanks to Monte Carlo simulations we can study how efficient was our detector, i.e. the study how many candidates of coherent ψ(2S) we have lost due to the imperfection of the detector. This is determined by the so-called acceptance and efficiency and in this Research Project it was computed as a function of the run number. Using the following equation:

$$(\text{Acc x Eff}) = \frac{\#\text{reconstructed events in y}}{\#\text{generated events in y}}, \tag{5.2}$$

where in the numerator is the number of reconstructed events per run and in the denominator is the number of the generated events per run, we obtain the (Acc x Eff) per each run. For every decay channel of ψ(2S) the results from (Acc x Eff) can be seen on the following figures 5.21 and 5.22.

We were interested in the dependence of the yield of coherent ψ(2S) on different rapidity ranges. It is nicely demonstrated on Fig. 5.16, 5.17, 5.18 and 5.19 where is depicted how is this variation of the rapidity range reflected on the reconstructed and generated invariant mass of the ψ(2S) and on its transverse momentum p_T. The consequence of this variation can be clearly seen on different results from (Acc x Eff), see Figs. 5.21, 5.22 which can serve as one of the tools to estimate the systematic uncertainty on the extraction of the signal.

5.10 Luminosity

We also analysed the luminosity of the trigger and we obtained $\mathcal{L}_{int} = 119,742\ \mu\text{b}^{-1}$, see Fig. 5.23. The underlying concepts on luminosity determination at ALICE are explained in [26]. The luminosity is corrected for the pile-up of the trigger used for the reference cross section. This pile-up correction should not be confused with the one mentioned in the next section.

5.11 Determination of the cross section

The importance of this analysis consists in the measurement of the cross section since this can help to scrutinised theoretical models trying to describe the gluon distribution in Pb nuclei at small-x. The differential cross section is determined from the following equation:

$$\frac{\mathrm{d}\sigma^{\text{coh}}_{\psi(2\text{S})}}{\mathrm{d}y} = \frac{N^{\text{coh}}_{\psi(2\text{S})}}{(\text{Acc} \times \epsilon)_{\psi(2\text{S})} BR(\psi(2\text{S}) \to \pi^-\pi^+\text{J}/\psi)\mathcal{L}_{int}\Delta y}, \tag{5.3}$$

where $N^{\text{coh}}_{\psi(2\text{S})}$ is the coherent yield of the ψ(2S) decaying in 4 particles, see Fig. 5.8. The yield from the direct decay channel also contains the backgrounds from the interaction of $\gamma\gamma \to \mu^+\mu^-$.

The (Acc$\times\epsilon$) is the acceptance and efficiency product, where are included the following computations which serve as a corrections to the final (Acc $\times$ ϵ):

1. (Acc $\times$ Eff) - the acceptance and efficiency product from the Monte Carlo simulation, see Figs. 5.21, 5.22. However as was already mentioned above, the trigger description in MC is wrong and must be reconstructed again.

2. (Acc $\times$ Eff) from the trigger.

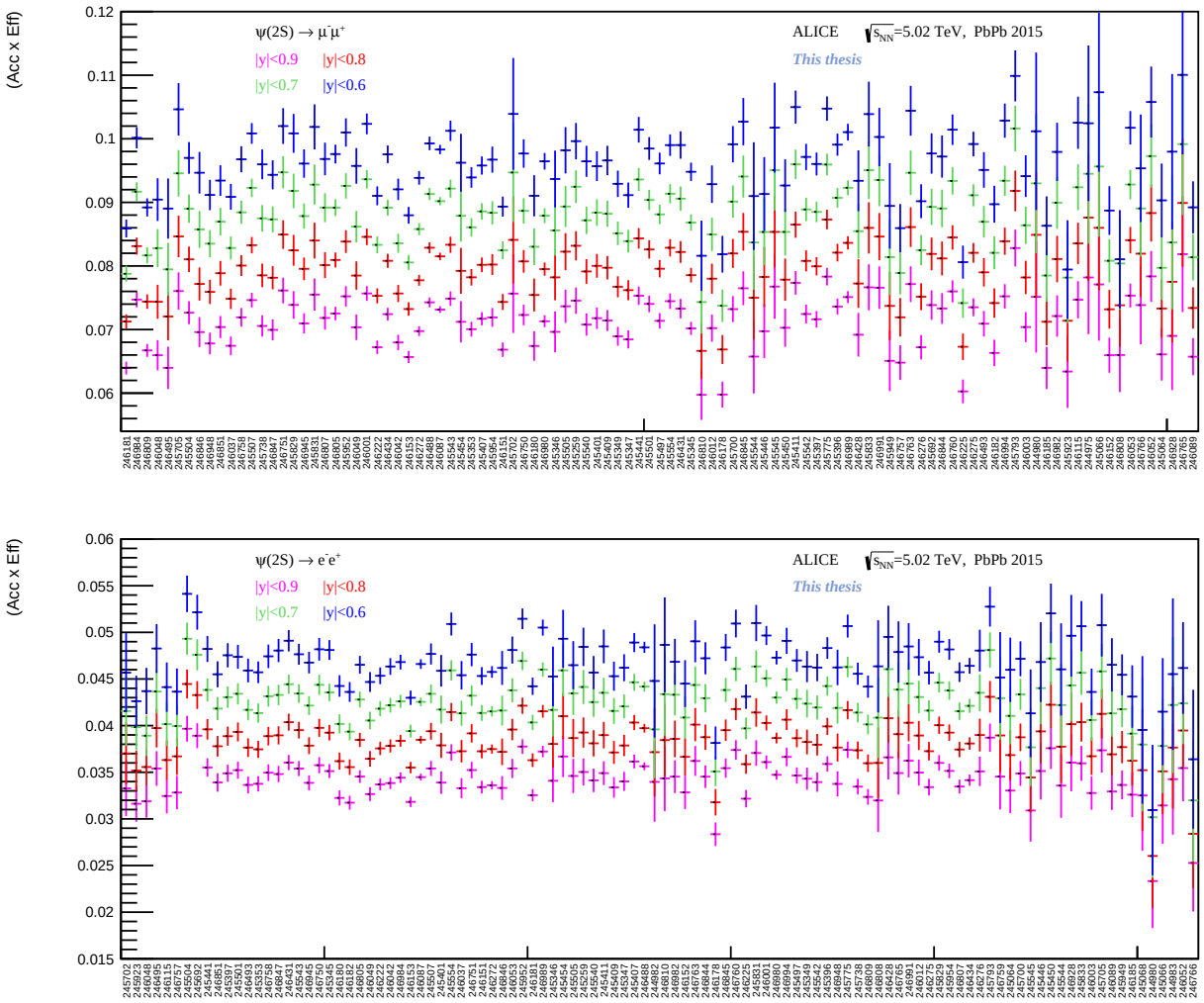

Figure 5.21: (Acc x Eff) per each run. Upper panel: The direct decay channel of the ψ(2S) into muons. Lower panel: The direct decay channel of the ψ(2S) into electrons.

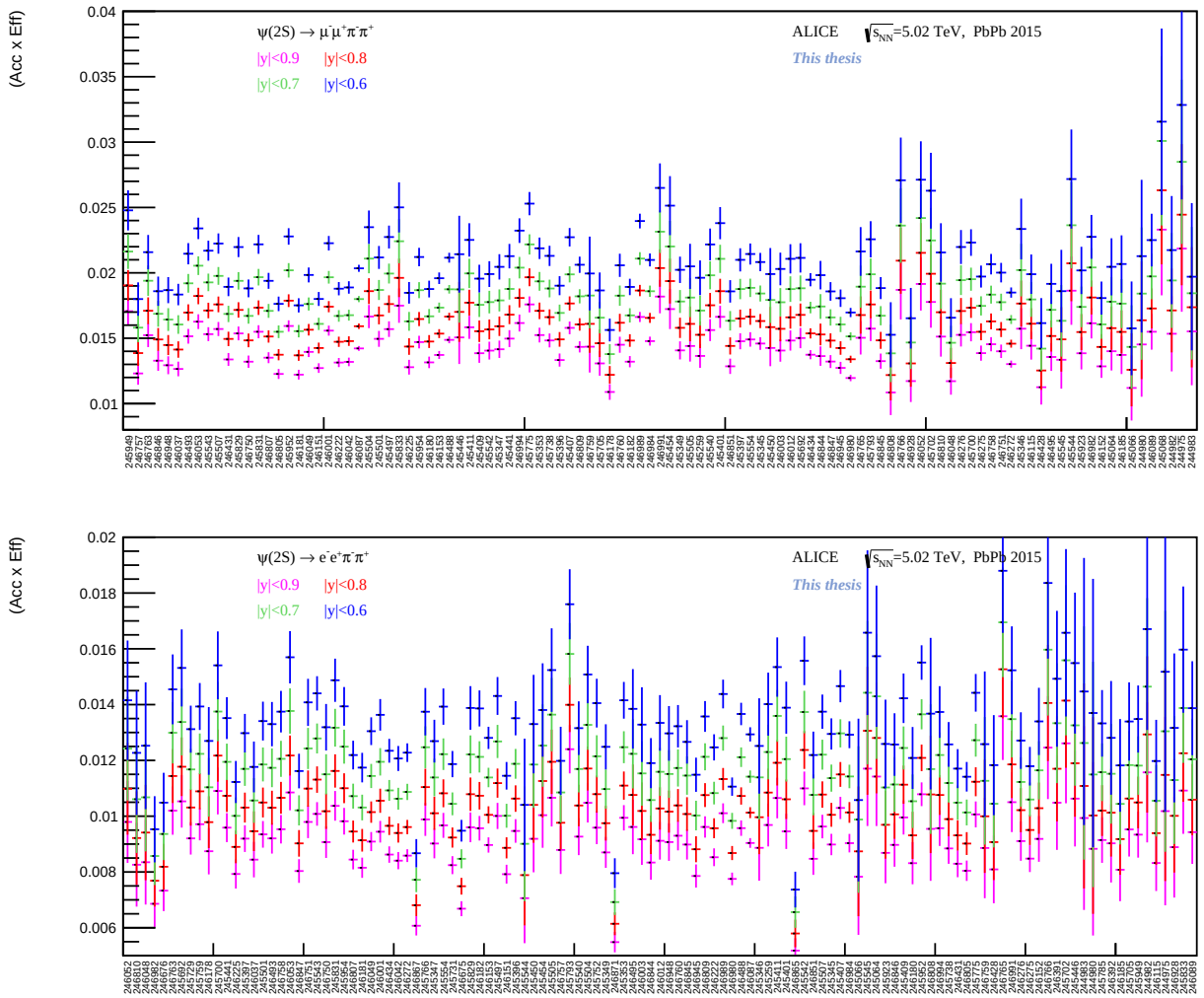

Figure 5.22: (Acc x Eff) per each run. Upper panel: The decay channel of the ψ(2S) into pions and muons. Lower panel: The decay channel of the ψ(2S) into pions and electrons.

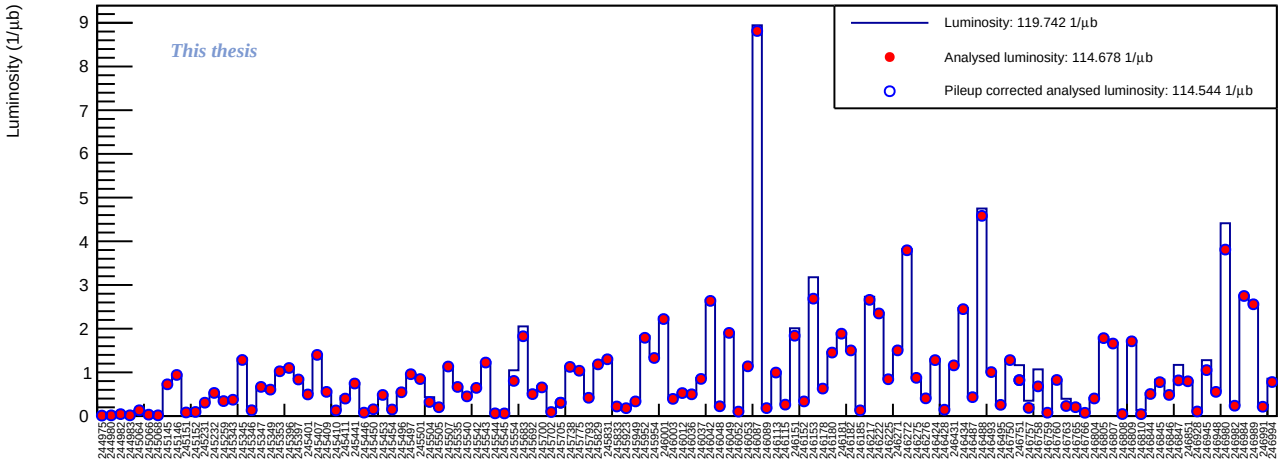

Figure 5.23: The integrated luminosity run-by-run.

3. (Acc $\times$ Eff) CTrue - the pile-up effects.

The BR(ψ(2S) $\rightarrow \pi^-\pi^+$J/ψ) is the branching ratio of the four product decay channel (for the direct decay channel it is BR(ψ(2S) $\rightarrow l^-l^+$), where l is either electron or muon), see Tab. 2.1 for the values of the BR. Finally, $\mathcal{L}_{int}$ is the integrated luminosity, see Fig. 5.23 and Δy is the given rapidity range, which is in this case $|y| < 0.9$, i.e. the mid-rapidity.

As can be seen, we have prepared almost everything for the final measurement of the cross section. Because of the problems which were already mentioned in Chap. 4, the incorrect reconstruction of the TOF trigger elements and thus its implementation in the simulation MC was also incorrect, unfortunately we cannot estimate the cross section in this Research Project since this will give us wrong results. Although the mentioned problems are solved now, as a consequence the data have to be reprocessed again, but after this we will be able to calculate the $\mathrm{d}\sigma^{\mathrm{coh}}_{\psi(2\mathrm{S})}/\mathrm{d}y$ relatively fast since we have prepared the necessary tools.

Chapter 6

Discussion and Summary

The main purpose of the analysis presented in this Research Project was to study coherent photoproduction of the vector meson $\psi(2S)$ in ultra-peripheral Pb–Pb collisions at the LHC in order to investigate the behaviour of the gluon distribution of lead nuclei at small x.

A great work in this field has been done by the H1 and ZEUS Collaborations analysing data at HERA [5]. Although the LHC was not constructed to perform this kind of physics, ultra-peripheral collisions together with the large energies which can be achieved in this facility give a great opportunity to continue the investigation of QCD phenomena. The centre-of-mass energy in Run 2 reached $\sqrt{s_{\mathrm{NN}}} = 5.02$ TeV in Pb–Pb collisions which means that coherently produced $\psi(2S)$ at mid-rapidity are sensitive to $x \sim 10^{-4}$ what is indeed a powerful tool to study the gluon distribution in lead nuclei. There exist theoretical predictions which try to describe these distributions and thus may explain the cause of interesting QCD phenomena such as shadowing and saturation. These models have to be verified against measurements of the cross section of the photoproduction processes. This Project Research studies the necessary contributions to obtain the cross section, see Eq. 5.3. of the coherent photoproduction of the $\psi(2S)$.

First of all, the data taken from ALICE in Run 2 were collected and understood. We studied 4 different decay channels of the $\psi(2S)$ charmonium: the direct one, $\psi(2S) \to l^- l^+$, where l stands for lepton and it can be either electron or muon. The other two studies were the decay of $\psi(2S)$ into 4 products, i.e. $\psi(2S) \to \mathrm{J}/\psi\pi^-\pi^+$, where $\mathrm{J}/\psi \to l^- l^+$. The resulting coherent yields of $\psi(2S)$ can be seen in Fig. 5.8 for the 4-product decay channel and in Fig. 5.11 and 5.12 for the direct decay channel. although in this case the main contribution to the coherent yield is from $\gamma\gamma \to \mu^-\mu^+$. To check that we really understand the data and we used the correct cuts, which can be found in Tab. 5.3 and 5.4, we used the Monte Carlo simulations.

We reconstructed the coherent yield of $\psi(2S)$ from simulations of the collision of Pb–Pb which were folded with the simulated ALICE detector, see Figs. 5.16, 5.17, 5.18 and 5.19. Then we analysed the simulation of the generated yield of $\psi(2S)$ in a given rapidity range, i.e. the simulation of a collision which was not influenced by the imperfection of the detector. Dividing these yields, reconstructed over generated, we studied the acceptance and efficiency product, i.e. how many event candidates we lost due to the imperfection of the detector. The results run-by-run can be seen for each decay channel in Figs. 5.21 and 5.22. We studied the dependence of the yield on variations of the ranges of rapidity and transverse momenta p_T which was consequently reflected on the variation of the (Acc $\times$ Eff).

We also calculated the integrated luminosity and we estimated its value to $\mathcal{L}_{int} = 119,742\ \mu\mathrm{b}^{-1}$, see Fig. 5.23.

This Research Project prepared all necessary tools for the final measurement of the cross section of the coherent photoproduction of a ψ(2S) off a lead nucleus at mid-rapidity, see Eq. 5.3. Unfortunately, due to the problems which were beyond us to solve them, we were not able to calculate the cross section $\mathrm{d}\sigma^{\mathrm{coh}}_{\psi(2S)}/\mathrm{d}y$. The problem was that during 2017 it was discovered that the reconstruction of the TOF trigger inputs was incorrect and thus its implementation in the MC simulation was also wrong. Now, after the implementation of the corrections, the test data confirm that both problems have been solved and in the following months the data will be reprocessed and MC simulations will be reconstructed again. When new data will be at our disposal, the estimation of the cross section will proceed fast since in this Research Project we have prepared all necessary tools. This result will be an important contribution towards verifying the correctness of theoretical models describing shadowing. Our estimation of $\mathrm{d}\sigma^{\mathrm{coh}}_{\psi(2S)}/\mathrm{d}y$ at mid-rapidity with higher energies reached in Run 2 together with the results from forward rapidity [21] will complement the measurement of the cross section, see Fig. 4.2, and might tell us something more about the origin of shadowing.

Bibliography

[1] A. J. Baltz. The Physics of Ultraperipheral Collisions at the LHC. *Phys. Rept.*, 458:1–171, 2008.

[2] Carlos A. Bertulani, Spencer R. Klein, and Joakim Nystrand. Physics of ultra-peripheral nuclear collisions. *Ann. Rev. Nucl. Part. Sci.*, 55:271–310, 2005.

[3] J. J. Aubert et al. Experimental Observation of a Heavy Particle J. *Phys. Rev. Lett.*, 33:1404–1406, 1974.

[4] K. A. Olive et al. Review of Particle Physics. *Chin. Phys.*, C38:090001, 2014.

[5] H. Abramowicz et al. Combination of measurements of inclusive deep inelastic $e^{\pm}p$ scattering cross sections and QCD analysis of HERA data. *Eur. Phys. J.*, C75(12):580, 2015.

[6] Nestor Armesto. Nuclear shadowing. *J. Phys.*, G32:R367–R394, 2006.

[7] K. Aamodt et al. The ALICE experiment at the CERN LHC. *JINST*, 3:S08002, 2008.

[8] Betty Bezverkhny Abelev et al. Performance of the ALICE Experiment at the CERN LHC. *Int. J. Mod. Phys.*, A29:1430044, 2014.

[9] 3D ALICE schematic - with description. `https://aliceinfo.cern.ch/Figure/node/3400`. Accessed: 2017-20-09.

[10] Jaroslav Adam et al. J/ψ suppression at forward rapidity in Pb-Pb collisions at $\sqrt{s_{NN}} = \mathbf{5.02}$ TeV. *Phys. Lett.*, B766:212–224, 2017.

[11] P Cortese et al. ALICE: Physics performance report, volume I. *J. Phys.*, G30:1517–1763, 2004.

[12] P Cortese et al. ALICE: Physics performance report, volume II. *J. Phys.*, G32:1295–2040, 2006.

[13] F. Antinori. The Alice inner tracking system. *Nucl. Instrum. Meth.*, A511:215–220, 2003.

[14] ITS sketch. `http://aliceinfo.cern.ch/ITSUpgrade/`. Accessed: 2017-20-09.

[15] Andrea Agostinelli. *Vector meson photoproduction in ultra-peripheral heavy ion collisions with ALICE at the LHC*. PhD thesis, Bologne U., 2014.

[16] Christian Lippmann. Particle identification. *Nucl. Instrum. Meth.*, A666:148–172, 2012.

[17] J Daniel Tapia Takaki and O Villalobos Baillie. *Physics performance studies for the ALICE experiment at the CERN LHC*. PhD thesis, Birmingham U., Birmingham, UK, 2008. Presented on 27 Jan 2008.

[18] Biswarup Paul and Sukalyan Chattopadhyay. *Charmonium studies at LHC energies using the ALICE Muon Spectrometer*. PhD thesis, HBNI, Mumbai, May 2015. Presented 15 Sep 2015.

[19] Betty Abelev et al. Coherent J/ψ photoproduction in ultra-peripheral Pb-Pb collisions at $\sqrt{s_{NN}} = 2.76$ TeV. *Phys. Lett.*, B718:1273–1283, 2013.

[20] E. Abbas et al. Charmonium and e^+e^- pair photoproduction at mid-rapidity in ultra-peripheral Pb-Pb collisions at $\sqrt{s_{\rm NN}}$=2.76 TeV. *Eur. Phys. J.*, C73(11):2617, 2013.

[21] E. L. Kryshen. Photoproduction of heavy vector mesons in ultra-peripheral Pb-Pb collisions. *Nucl. Phys.*, A967:273–276, 2017.

[22] V. P. Goncalves, B. D. Moreira, and F. S. Navarra. Investigation of diffractive photoproduction of J/Ψ in hadronic collisions. *Phys. Rev.*, C90(1):015203, 2014.

[23] G. Sampaio dos Santos and M. V. T. Machado. On theoretical uncertainty of color dipole phenomenology in the J/ψ and Υ photoproduction in pA and AA collisions at the CERN Large Hadron Collider. *J. Phys.*, G42(10):105001, 2015.

[24] T. Lappi and H. Mantysaari. J/ψ production in ultraperipheral Pb+Pb and p+Pb collisions at energies available at the CERN Large Hadron Collider. *Phys. Rev.*, C87(3):032201, 2013.

[25] V. Guzey, E. Kryshen, and M. Zhalov. Coherent photoproduction of vector mesons in ultraperipheral heavy ion collisions: Update for run 2 at the CERN Large Hadron Collider. *Phys. Rev.*, C93(5):055206, 2016.

[26] E. Kryshen. Luminosity determination for ultra-peripheral triggers in Pb-Pb at $\sqrt{s_{NN}} = 5.02$ TeV. *Analysis Note*. Accessed: 2017-12-12.